Geomorphology 403 (2022) 108173

Contents lists available at ScienceDirect

Geomorphology

journal homepage: www.journals.elsevier.com/geomorphology

Storm characteristics dictate sediment dynamics and geomorphic changes in mountain channels: A case study in the Italian Alps

Vittoria Scorpio [a,b,*], Marco Cavalli [c], Stefan Steger [a], Stefano Crema [c], Francesco Marra [d], Mattia Zaramella [e], Marco Borga [e], Lorenzo Marchi [c], Francesco Comiti [f]

[a] Institute for Earth Observation, Eurac Research, 39100 Bolzano, Italy
[b] Department of Chemical and Geological Sciences, University of Modena and Reggio Emilia, 41125 Modena, Italy
[c] Research Institute for Geo-hydrological Protection, National Research Council (CNR IRPI), Padova, Italy
[d] Institute of Atmospheric Sciences and Climate, National Research Council (CNR ISAC), Bologna, Italy
[e] Department of Land, Environment, Agriculture and Forestry, University of Padova, Padova, Italy
[f] Faculty of Science and Technology, Free University of Bozen-Bolzano, Bolzano, Italy

ARTICLE INFO

Keywords:
Basin-scale analysis
Flood magnitude
Sediment connectivity
Coupled debris flow
Channel widening and elevation changes in the river corridor
DEM of difference (DoD)

ABSTRACT

In mountain environments, the coupling of hillslopes processes with the channel network during extreme events is of great importance for rivers dynamics, as debris flows and landslides are among the most important sources of sediments. The Stolla Creek (40 km^2 drainage area, South Tyrol, Italy) is a confined and partly confined mountain channel that was affected by an extreme flood in August 2017, followed by a smaller event in August 2020. The geomorphic effects of the two floods were investigated both in the main channel and over the entire basin with the aim to assess the impacts of the lateral sediment connectivity to the channel response and to the event-scale sediment export.

An integrated approach was applied, including radar rainfall estimation, hydrologic-hydraulic analysis, analysis of morphological changes and sediment delivery to the stream network. Hillslope and channel processes were mapped and characterized by using geomorphological analysis of multitemporal orthophotos and Digital Terrain Models. Debris-flow connectivity to the main channel was derived by combining field evidence and GIS-based analysis.

The 2017 flood was caused by rainfall with a short duration (6 h) and a rainfall intensity exceeding 45 mm/h. More than 600 debris flows were triggered in the Stolla basin, and the main channel experienced widening (width ratio between 1.3 and 4.9) through bank erosion and overbank deposition. Widening was accompanied by aggradation in the river corridor up to 1.2 m or incision down to −2.2 m. The 2020 flood was characterized by lower rainfall intensity (max 17 mm/h) and a longer duration (48 h), and debris flows were not triggered. The moderate magnitude of the 2020 flood peak did not lead to channel widening, but marked bed incision (up to −1.4 m) occurred in the reaches where aggradation took place during the 2017 event. In both flood events, limited volumes of sediments were exported from the catchment outlet.

Overall, our results highlight how structural connectivity at the basin scale determines the potential sediment cascades linking hillslopes to channels but time-varying functional connectivity – driven by hydrological drivers as rainfall intensities and durations – eventually control the actual sediment transport effectiveness both on hillslopes and along the channel.

1. Introduction

Several heavy precipitation events have affected Europe over the last years (Llasat et al., 2010; Boudevillain et al., 2011; Tarolli et al., 2012; Nardi and Rinaldi, 2015; Santo et al., 2015; Lucía et al., 2018). Such events induced geomorphological impacts on channels, valley bottoms, and adjacent hillslopes, which consisted in channel widening, changes in bed level, channel avulsions, mass movements of varying types, as well as recruitment and transport of large wood (Morche et al., 2006; Hauer and Habersack, 2009; Krapesch et al., 2011; Grove et al., 2013;

* Corresponding author at: Department of Chemical and Geological Sciences, University of Modena and Reggio Emilia, 41125 Modena, Italy.
E-mail address: vittoria.scorpio@unimore.it (V. Scorpio).

https://doi.org/10.1016/j.geomorph.2022.108173
Received 6 May 2021; Received in revised form 8 February 2022; Accepted 14 February 2022
Available online 23 February 2022
0169-555X/© 2022 The Authors. Published by Elsevier B.V. This is an open access article under the CC BY-NC-ND license (http://creativecommons.org/licenses/by-nc-nd/4.0/).

Fryirs et al., 2015; Lucía et al., 2015; Righini et al., 2017). In mountain environments, landslides and debris flows are among the most important sources of sediment supply and the prevalent mechanisms for delivering sediments to the valley bottoms (Schuerch et al., 2006; Brardinoni et al., 2015; Stoffel et al., 2016; Schopper et al., 2019; Cislaghi and Bischetti, 2019).

During extreme precipitation events, large amounts of sediment and large wood are eroded and transferred from hillslopes and low-order streams to the main channel network in a short time (Schuerch et al., 2006; Thompson et al., 2016; Shmilovitz et al., 2020). Indeed, the coupling/decoupling of sediment sources with channels – also referred to as lateral sediment connectivity – is of the utmost importance for understanding sediment dynamics in rivers (Beylich and Brardinoni, 2013; Brardinoni et al., 2015; Bracken et al., 2015; Rinaldi et al., 2016; Wohl et al., 2019). The rate of sediment transport, storage and reworking in sediment cascades is controlled by the strength of coupling between neighboring storages on hillslopes and the connectivity to the streams (Fryirs, 2013; Messenzehl et al., 2014). Importantly, most sediment transfer occurs in form of pulses associated to extreme events, under the control of landscape morphological setting and of anthropic

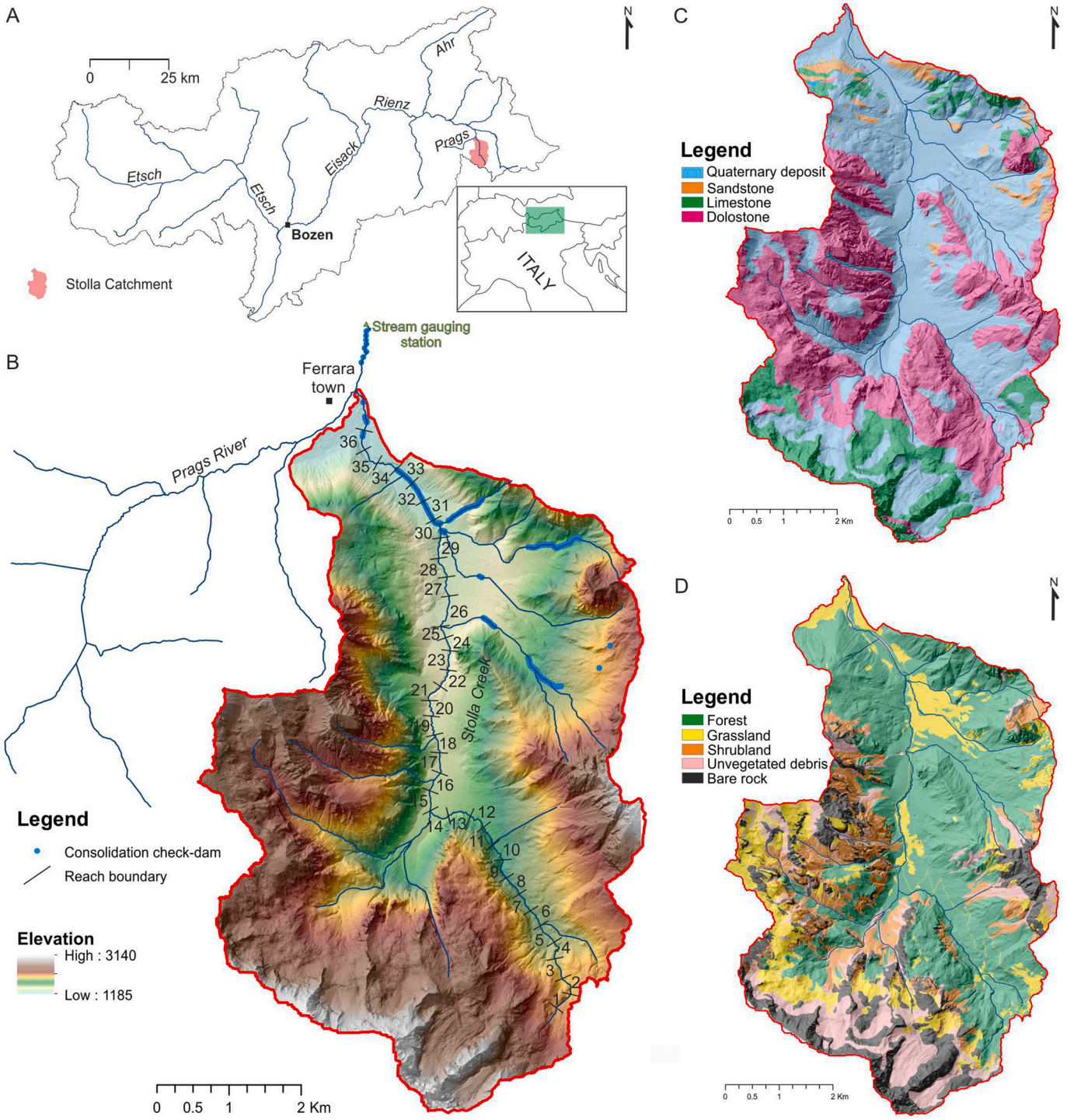

Fig. 1. Location map of the Stolla catchment (A); location of studied reaches (B); geological sketch of the Stolla catchment (C); land-use map in the Stolla catchment (D).

pressures and management (Cavalli et al., 2019; Fryirs, 2013; Thompson et al., 2016; Scorpio et al., 2016; Llena et al., 2019).

In general, floods represent the primary form of pulse disturbance along rivers, whereas climate change or land-use change can be considered additional disturbances (Fryirs, 2017; Liébault et al., 2005; Scorpio and Piégay, 2021). Floods of varying magnitude, frequency and duration cause different consequences in channels depending on channel characteristics, the structural connectivity of the system (Hooke, 2015) and on the sensitivity of the landscape, intended as "the likelihood that a given change in the controls of a system will produce a sensible, recognizable and persistent response" (Brunsden and Thornes, 1979); for more extensive definitions see also Fryirs (2017). After any disturbance event, the sensitivity of a system may shift, some systems may become more sensitive to future disturbances, others may become more resilient (Phillips, 2009; Schumm, 1991; Fryirs, 2017; Piégay et al., 2020). Several studies have focused on evaluating the structural connectivity between landslides and debris flows and the channel network during extreme geomorphic events (Harvey, 2001; Schmidt and Morche, 2006; Tiranti et al., 2016; Surian et al., 2016; De Walque et al., 2017; Cavalli et al., 2017), but fewer works have examined channel response to multiple high flows (Bertoldi et al., 2010; Surian et al., 2009; Eagle et al., 2021) under the perspective of different levels of functional connectivity (Wainwright et al., 2011).

The present study analyses the geomorphic effects associated with two hydrometeorological events presenting different magnitude and which occurred in August 2017 and August 2020 in the Stolla Creek basin, located in the Eastern Italian Alps. The specific aims of this study can be summarized as follows: i) to quantify and compare channel morphological changes induced by two contrasting storm events; ii) to provide a basin-scale understanding of such channel morphological changes; iii) to explore whether different types of channel widening processes (bank erosion and overbank deposition) occurred under different conditions; iv) to assess the role of structural and functional sediment connectivity on sediment transfer and channel response.

2. Study area

The Stolla creek basin is located in the eastern part of South Tyrol (Autonomous Province of Bozen-Bolzano, Italian Alps; Fig. 1A) and covers an area of 40 km^2. Mean annual precipitation and mean annual temperature are 860 mm and 5.5 °C, respectively (Stockner, 2019). The Stolla catchment presently does not host glaciers, but it was entirely glaciated during the Pleistocene. The highest peak in the catchment (Hohe Gaisl/Croda Rossa) has an elevation of 3146 m a.s.l., and the catchment outlet is located at 1185 m a.s.l., where the Stolla Creek (11.5 km in length) joins the Prags/Braies River. This latter is a tributary of the Rienz/Rienza River (Fig. 1A and B), which in turn belongs to the Etsch/Adige river basin.

The geological substrate of the Stolla catchment is mainly characterized by sedimentary rocks. Limestones, dolostones, as well as alternations of marls and limestones outcrop at the higher elevations (Fig. 1C). At lower elevations, closer to the outlet, the basin is composed of alternating limestones and sandstones. Bedrock is covered by different types of deposits. An extensive Quaternary cover of till and fluvioglacial deposits is present, widely reworked by colluvial and alluvial processes. The rockslopes undergo intense weathering and erosion processes which feed large volumes of loose sediments to the steep talus slopes and cones at the feet of the rockwalls. Such talus landforms are preferential initiation zones for debris flows in the Dolomites (Marchi et al., 2008; Gregoretti et al., 2016) because, beside the availability of loose sediment on steep (>30°) slopes, concentrated water runoff generated from the rockwalls above represents an effective triggering mechanism. Indeed, debris flows in the Stolla basin are well known to occur quite frequently during intense summer storms.

The catchment hosts conifer forests (48% of the basin area) composed of Norway spruce (*Picea abies*) and silver fir (*Abies alba*) in the middle and lower parts, up to the tree line (about 2200–2300 m a.s.l., Fig. 1D). At higher elevations, vegetation mainly consists of grasslands (15% of the basin area) and shrublands (11% of the basin area) composed of mugo pine (*Pinus mugo*). Unvegetated areas – bedrock outcrops and bare sediments – occupy about 26% of the basin area. In the catchment, there are only a few buildings, mostly for mountain tourism.

The channel network presents a low drainage density (Fig. 1B), as very few perennial tributaries flow into the Stolla. The Stolla main channel is single-thread, mostly confined (following the classification proposed in Rinaldi et al., 2015) in the upper part, whereas it is characterized by an alternation of confined and partly confined reaches in the middle and lower sectors.

The river network in the Stolla catchment features a very limited presence of artificial structures, except in 4 tributaries and the most downstream reaches of the Stolla Creek, which are stabilized by a sequence of grade-control structures (consolidation check-dams, Fig. 1B).

The Stolla catchment was affected by two storms on 5th August 2017, and on 31st August 2020. As a consequence of the short-duration a very intense precipitation in August 2017 (hereafter event I), the Stolla Creek and the Prags river downstream of the Stolla-Prags confluence increased rapidly in flow discharge. Large volumes of sediments were mobilized and transferred downstream from talus slopes in the form of debris flows over the entire Prags basin (Minute et al., 2019, Fig. 2). In contrast, the August 2020 storm event was characterized by higher cumulative precipitation than in 2017, but rainfall intensities were markedly lower. In 2020 no mass movements were triggered in the basin.

Immediately after both events field surveys were carried out. The deposits created by the flood events consist of stratified layers composed of clast-supported pebbles, cobbles and boulders, poorly to moderately sorted, moderately imbricated (Fig. 2G). Matrix was rich in coarse sand. Clasts, generally subangular or moderately rounded, were made of carbonate lithology. Locally, poorly imbricated boulders (maximum diameter around 1 m), organized in clast-supported and poorly sorted facies, were structured in depositional lobes (Fig. 2H). Analyzing the characteristic of the deposits, bedload transport was the main sediment transport process that occurred in the Stolla channel. Nonetheless, debris flooding (Brenna et al., 2020; Church and Jakob, 2020) occurred in some reaches during the 2017 event.

3. Materials and methods

This study is based on an integrated approach that includes field surveys, remote sensing analysis, geomorphometric analysis, radar rainfall estimation, rainfall-runoff modelling, and statistical analysis of the data related to the morphological response of the channel system.

For the event I a more complete analysis of the channel and hillslopes dynamics were performed (Table 1). In contrast, for event II the analyses focused mainly on the upper segment of the Stolla channel (Table 1 and see Section 3.3.2), since no geomorphological effects (debris flows, landslides) were observed along the hillslopes.

3.1. Hydrological-hydraulic analysis

3.1.1. Spatial distribution of rainfall and recorded flood hydrographs

Raw radar data from the Macaion weather radar were provided at 5-minute temporal resolution by the Autonomous Province of Bozen-Bolzano. The data were already processed for removing effects due to non-precipitating echoes by use of a Doppler-based technique. The data were then corrected for estimation errors due to wet radome attenuation (Marra et al., 2014), partial (up to 70%) blockage of the radar beam due to orography (Pellarin et al., 2002; Marra et al., 2014), attenuation of the beam due to heavy rain (Marra and Morin, 2015), and vertical variations of the radar reflectivity (Marra and Morin, 2015). Reflectivity

Fig. 2. Debris flow and alluvial channel processes in the Stolla catchment after event I. Debris flow (A); active debris fans connected to the Stolla channel (B); disconnected debris flow (C); toe erosion processes (D); bank erosion (E); overbank deposition on the former floodplain (F); details of the overbank deposits (G); depositional lobe (H).

values exceeding 56.5 dBZ (about 150 mm/h) were set to this cap value to reduce the possible impact of hail. Rain rate (R) was derived from radar reflectivity (Z) using a Z-R power law relation: $Z = 400 \cdot R^{1.4}$ using the maximum reflectivity observed along the vertical for elevation angles between 1° and 5° (Marra et al., 2014). Cartesian maps at 1 km horizontal resolution were then created. Rain gauge measurements were assimilated to account for radar estimation bias using a multi-quadratic spatial dependent adjustment (multi-quadratic parameter = 0.2; Martens et al., 2013; Amponsah et al., 2016). The adjustment was implemented based on 13 stations surrounding the study catchment and using the total event rainfall depth in order to reduce the possible impact of the scale-mismatch between the rain gauge and the radar sampling volume (Villarini et al., 2008). Independent leave-one-out validation shows a root mean square error of 5.2 mm over the event storm amounts (~7% of the average rain gauge amount) and a correlation coefficient of 0.88, meaning that only ~22.5% of the observed variance can be related to estimation errors. The final radar product was thus able to well represent both the storm spatial structure and the total rainfall volumes

Table 1
List of the methods applied to investigate the floods in 2017 (event I) and 2020 (event II).

Analysis/method	Flood of 5th August 2017 (event I)	Flood of 31st August 2020 (event II)
Radar rainfall estimation	x	x
Post-flood reconstruction of peak discharges and rainfall-runoff modelling	x	
Mapping of channel morphology before and after the flood event	x	x[a]
Assessment of planimetric morphological changes of the channel, islands and floodplains	x	
Assessment of elevation changes in river corridor (DoD technique)	x	x[a]
Inventory mapping of debris flows and toe erosions	x	
Assessment of sediment supplied to the main channel by debris flows (DoD technique)	x	
Sediment storage variation assessment in the Stolla channel	x	x[a]
Statistical analysis of the factors influencing channel response to floods	x	

[a] Only in the upper segment (reaches from 1 to 14, see Fig. 1B and Section 3.3.2).

(0.2% relative bias).

A stream gauge is located on the Prags River, about 1800 m downstream of the confluence with the Stolla Creek (Figs. 1, 4). Discharge data were provided by the Autonomous Province of Bozen-Bolzano and a flood hydrograph at Braies station was reconstructed for both flood events by means of a flow rating curve. The reconstruction can be considered reliable since none of the events flooded over the section at the station.

3.1.2. Assessment of the rainfall severity

The assessment of the rainfall return time is based on a rainfall regional frequency assessment procedure, available for the area, which relies on the availability of annual maximum series of rainfall depth for different rainfall durations comprised between 1 h and 24 h (Destro et al., 2017). The procedure relies on the General Extreme Value (GEV) distribution (Jenkinson, 1955) which is used together with a simple scaling hypothesis to derive rainfall depth, duration and frequency (DDF) relationship at any site in the area. For an analysis of the scale-invariance property in the study area see Borga et al. (2005).

3.1.3. Flood response modelling

A spatially distributed hydrological model, termed Kinematic Local Excess Model (KLEM; Borga et al., 2007; Amponsah et al., 2016) was applied to analyze the flood response and to compute the flood peak discharge for the different channel reaches. It combines runoff generation modelling by means of the Probability Distributed Model (PDM; Moore, 2007) with a network-based hillslope and channel runoff propagation model. Spatial variation in runoff generation modelling is driven by maps of geological formations, after identification of two main classes (Fig. 1C) (deposits and rocky areas, including limestone, sandstone and dolostone) for which different parameter sets are considered. The model was calibrated based on the flood hydrograph available at the Prags River stream gauge (Fig. 4). The hydrological model was verified by comparing model-simulated flood peaks with peak discharges reconstructed from high-water marks surveyed after the flood at a few ungauged cross sections (Amponsah et al., 2016). The KLEM model was then applied at the channel reach scale to compute peak discharge (and hence stream power).

3.2. Orthophotos and LiDAR-derived DTMs

Morphological changes caused by the two storm events in the Stolla basin were investigated by comparing multi-temporal orthophotos and DTMs surveyed in 2010–2014, 2017 and 2020.

A 2010 LiDAR DTM (point cloud density 4 points m^{-2}) was made available by the Autonomous Province of Bolzano-Bozen, along with orthophotos of 2014 (0.2 m spatial resolution).

The post – 2017 event orthophotos (0.15 m spatial resolution) and the DTM (point cloud density 29 points m^{-2}) were acquired during a LiDAR survey in October 2017.

New orthophotos (0.025 m spatial resolution) and LiDAR data (average point density about 100 points m^{-2}) were acquired in September 2020 using a drone flight (85 m average height).

All the bare ground point clouds were interpolated using the Natural Neighbor algorithm available in the ArcGIS software (ESRI ArcGIS ver.10.7) to generate three DTMs with a homogeneous resolution of 1 m. From the analysis on stable areas of known elevations, vertical accuracy of 0.35 m for the 2010 DTM, 0.20 m for the 2017 DTM and below 0.10 m for the 2020 DTM was estimated.

Orthophotos and DTMs in 2010, 2014 and 2017 cover the entire catchment, while orthophotos and DTM in 2020 only cover the upper Stolla channel (from reach 2 to reach 14, Fig. 1B).

3.3. Geomorphological analysis

3.3.1. Sediment supply from hillslopes and channel banks

The assessment of sediment supplied from hillslopes and channel banks to the Stolla Creek during event I was carried out by producing and analyzing a detailed debris flow and toe erosion (i.e., lateral fluvial erosion of colluvial deposits) inventory through field surveys, interpretation and comparison of orthophotos and DTMs taken before (orthophotos 2014 and DTM 2010) and immediately after the flood (orthophotos and DTM in 2017).

All debris flows (connected and disconnected from the Stolla channel) and toe erosions along the banks were mapped as polygons in a GIS software (ESRI ArcGIS ver.10.7).

Debris flows were mapped manually by following a geomorphological approach based on visually comparing the multitemporal orthophothos, DTMs and derived shaded relief maps (Fig. 3A, B, C, D). The obtained polygons were divided into two main zones: the initiation-propagation zone and the deposition zone. Initiation and propagation zones were merged because it was very difficult to distinguish the two processes and erosion occurred in most parts of the channels. Afterwards, the geomorphological interpretation was validated and, if necessary, corrected by comparing the debris flow polygons with the DoD map (Fig. 3E, DTM of difference, see Section 3.3.4). A detailed map of debris flows was thus obtained (Fig. 3F).

The coupling or decoupling of the debris flows with the Stolla channel was evaluated on the basis of field observations (Fig. 3G, H) carried out just after the storm event. More specifically if coarse sediment reached the main channel the related debris flow polygon was classified as connected and vice versa (Figs. 3G, F, 1SA).

Several morphometric variables relative to sediment sources area of the mapped debris flows were computed with the softwares ESRI ArcGIS ver.10.7 and SAGA GIS ver. 2.3.2. They encompass elevation, slope, contributing area, distance to the lower hierarchical stream order, topographic wetness index (TWI, Boehner et al., 2002), and cumulative rainfall during the event in 2017.

Empirical relationships between connected/disconnected release zones of debris flows and the morphometric variables were analyzed by means of conditional frequency plots (c.f. Brenning, 2008; Steger et al., 2016; Steger et al., 2021). These plots depict how the ratio between connected and disconnected debris flows varies across variable values. For instance, a conditional frequency of 0.3 (y-axis) observed for grassland areas (x-axis) shows that 30% of the inventoried debris flows

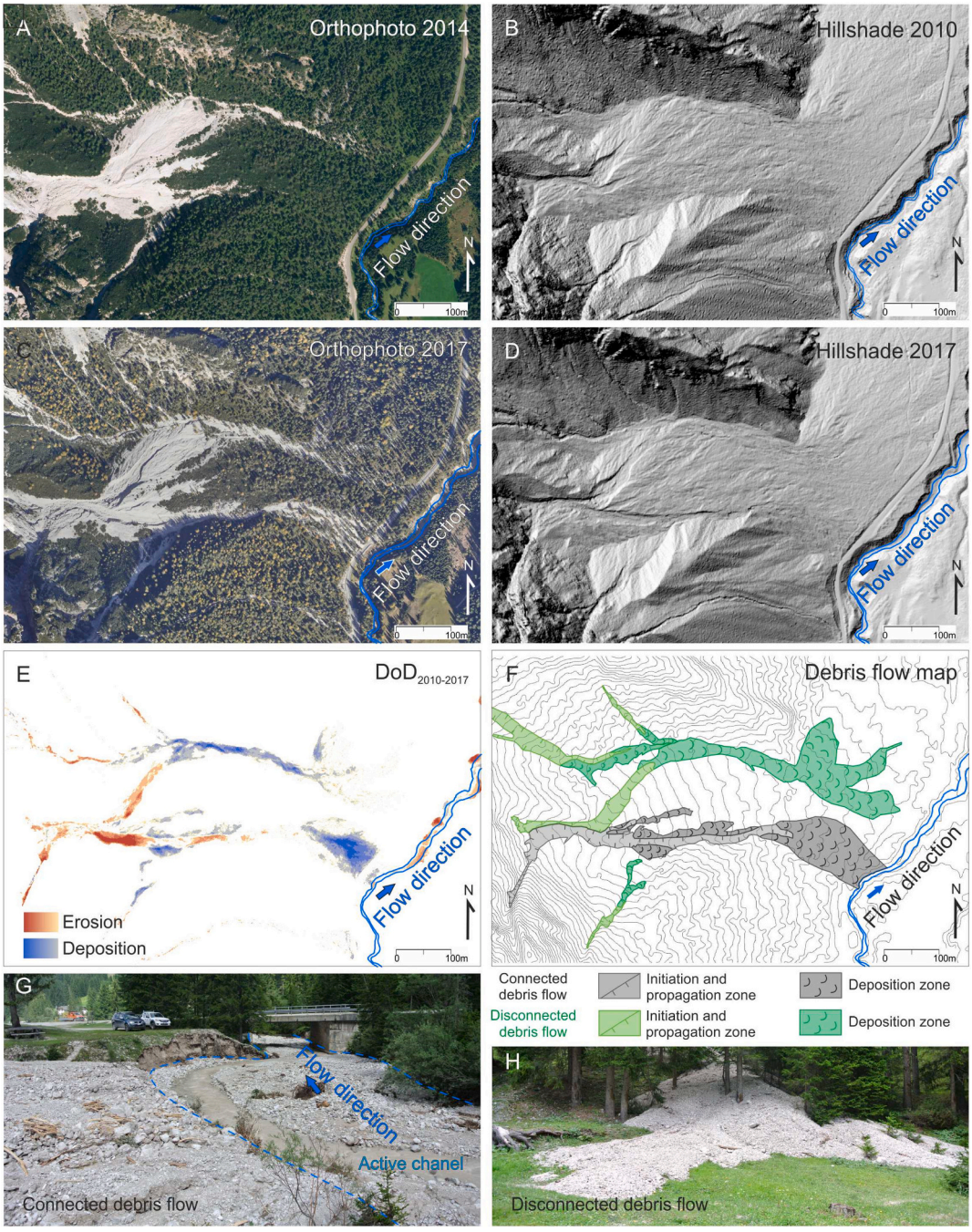

Fig. 3. Example of material used to map debris flows, to separate the initiation and propagation zones from the deposition zones and to classify the connected and the disconnected debris flows: orthophoto in 2014 and hillshade in 2010, before the event in 2017 (A, B); orthophoto and hillshade in 2017, after the event I in 2017 (C, D); map resulting from the DoD analysis (E); obtained map of the debris flows (F). Field analysis and examples of connected (G) and disconnected (H) debris flows.

are connected with the main channel while the remaining 70% of debris flow observations are unconnected. Due to the unbalanced number of observations in the total sample (87% of disconnected debris flows; 13% of connected debris flow), a conditional frequency of 0.13 depicts an equal-ratio-threshold that separates an overproportional occurrence of connected debris flow observations (>0.13) from a below-average conditional density of connected debris flow (<0.13). With reference to the previous example, a conditional frequency of 0.3 therefore points to a considerable over-representation of connected debris flows compared to unconnected ones in the area of interest (i.e. in this case grassland).

Finally, in order to provide a general picture of structural connectivity, a map of the sediment connectivity index (Cavalli et al., 2013) was computed, employing the SedInConnect software (Crema and Cavalli, 2018). The computation of IC, whose details can be found in the work by Cavalli et al. (2013) was performed on the 2010 DTM (1-m resolution) considering the Stolla channel as the target of the analysis. The obtained map was overlaid on the debris flow map to compare the connectivity index with connectivity classification performed in the field and to obtain averaged values of the connectivity index associated with each debris flow (Table 2).

3.3.2. River network segmentation

The Stolla channel was partitioned into 36 reaches (reaches are

Table 2
List of morphological and hydraulic variables evaluated for each reach. Flood I: 2017, flood II: 2020.

Parameter	Acr.	Description	Flood
Channel width before the flood (m)	W_{pre}	Median value of the lengths of a set of cross-sections spaded 10 m and intersecting the channel banks before the flood	I and II
Channel width after the flood (m)	W_{post}	Median value of the lengths of a set of cross-sections spaded 10 m and intersecting the channel banks after the flood	I and II
Width ratio (m/m)	Wr	Ratio between the channel width after the flood and channel width before	I and II
Area of widening	AW	Area of difference between the channel polygon after the flood and channel polygon before the flood. It corresponds with the area eroded by bank erosion processes of experiencing overbank deposition	I
Reach scale elevation modification in river corridor (m)	ΔH	Average elevation changes in river corridor at reach scale: net thickness of differences derived from the DoD analysis	I and II
Elevation modification in the area of widening (m)	ΔHw	Average vertical changes in the area of channel widening: average net thickness of differences derived from DoD analysis	I and II
Average incision in the river corridor(m)	ΔH_{Inc}	Average depth of lowering in the river corridor at reach scale, derived from the DoD analysis	I and II
Average aggradation in the river corridor	ΔH_{aggr}	Average depth of raising in the river corridor at reach scale, derived from the DoD analysis	I and II
Widening typology	$WType$	Main process for widening bank erosion (BE) or overbank deposition (OD)	I
Channel slope (°)	Sp	Channel slope estimated from the DTM 2010	I
Sinuosity index before the flood	SI_{pre}	Sinuosity index before the flood evaluated as the ratio between channel length and valley length (channel in 2014)	I
Sinuosity index after the flood	SI_{post}	Sinuosity index after the flood evaluated as the ratio between channel length and valley length	I
Planform morphology (pattern) before the flood	–	Channel planform morphology in 2014: S = sinuous; Str = straight	I
Planform morphology (pattern) after the flood	–	Channel planform morphology in 2017: SAB = sinuous alternate bars; S = sinuous; Str = straight	I
Islands area before the flood (m^2)	I_{pre}	Area of the islands in the reach before the flood (in 2014)	I
Island area after the flood (m^2)	I_{post}	Area of the islands in the sub-reach after the flood (in 2017)	I
Lateral migration (m)	$LatMig$	Median value of lateral migration of the channel center lines between 2014 and 2017. It is evaluated along cross-section spaced 10 m	I
	$LatMig_{max}$	Maximum lateral migration of the channel center lines between 2014 and 2017. It is evaluated along cross-section spaced 10 m.	I
Confinement index before the flood (m/m) (lateral confinement of the channel)	CI	Ratio between the alluvial plain width and the channel width before the flood (Rinaldi et al., 2013)	I
Confinement degree before the flood (m/m) (longitudinal confinement of the channel)	Cd	% of channel banks in contact with the hillslopes before the flood (Rinaldi et al., 2013)	I
Class of confinement before and after	–	C = confined; PC = partly confined; U = unconfined	I
Basin area (km^2)	Ba	Area of the basin feeding the reaches	–
Debris flow magnitude (m^2)	M_{df}	Volumes of sediments eroded in the coupled debris flow polygons	I
Sediment supply from toe erosions (m^2)	SS_{toe}	Volumes released to the main channel from toe erosions	I
Index of connectivity	IC	Relative sediment transport efficiency from upstream to downstream, calculated: i) as median value in the polygon of the debris flows classified as connected during the field trip analysis (when comparing values in the connected debris flows) and ii) in the release area of all debris flows (when comparing connected and disconnected debris flows) by using the index proposed by Cavalli et al. (2013).	I
Average cumulative rainfall (mm)	R	Average cumulative rainfall in the catchment draining the reaches	I
Peak discharge ($m^3\ s^{-1}$)	Q_{pk}	Peak discharge reconstructed in the reach by means hydrological modelling	I
Total stream power ($W\ m^{-1}$)	Ω	total stream power $\Omega = \gamma QS$; γ is the specific weight of water (Nm^{-3}), Q is the discharge ($m^3\ s^{-1}$), and S is channel slope (Bagnold, 1966; Magilligan, 1992; Knighton, 1999; Reinfelds et al., 2004)	I
Unit stream power ($W\ m^{-2}$)	ω	$\omega = \Omega/W_{pre}$	I

numbered in ascending order from upstream to downstream, see Fig. 1B) applying the approach proposed by Ferencevic and Ashmore (2012). The methodology mainly takes into account the changes in channel slope, but also the occurrence of discontinuities as confluences of tributaries, changes in lateral confinement and valley orientation (Rinaldi et al., 2013; Surian et al., 2016). This analysis was carried out by means of a 1-m resolution DTM derived from a LiDAR survey carried out in 2010 (see Section 3.2). Channel reach length ranges from 298 m to 350 m. The ratio between reach length and channel width ranges between 17 and 149 (median = 75) considering channel width before 2017, and between 12 and 76 (median = 34) referring to the width after the 2017 flood. For the analysis of the 2017 flood, all 36 reaches were considered. For the 2020 flood, only reaches 2 to 14 were analyzed (Fig. 1B) as this channel segment was the most severely affected in terms of changes. Also, downstream reaches were morphologically impacted by sediment cleaning operation a few days after the flood event.

3.3.3. Planform changes in the valley bottom

Planform changes in the Stolla river corridor (including active

channel, channel banks, floodplains and islands, Leopold and Marchand, 1968) induced by the two floods were assessed through field surveys and photointerpretation. The orthophotos interpretation was carried out using the ArcGIS software (ESRI ArcGIS ver.10.7) and it was based on the comparison of two sets of orthophotos taken before and after each flood.

For the analysis of event I, the 2014 orthophotos were used as highly representative of the channel before the event, because no geomorphically effective floods occurred between 2014 and August 2017. The 2017 orthophotos nicely captured the immediate post-flood conditions. The analysis of event II was based on the comparison of the same 2017 orthophotos against those acquired right after the 2020 flood.

Active channel, islands and alluvial plain margins were digitized as polygons from both pre- and post-flood orthophotos (Toone et al., 2012; Surian et al., 2016). Active channel was mapped including low-flow channels and unvegetated or scarcely vegetated bars. Woody vegetated islands were excluded from the active channel domain along with flooded areas without gravel deposits since they were not characterized by bedload transport. Alluvial plain margins included only recent and lowest terraces (in the case study: average elevation > 2 m above the average channel elevation), whereas higher and older terraces and alluvial fans were left out from the valley bottom.

Channel widths in 2014, 2017 and 2020 were estimated for each reach by using the FluvialCorridor toolbox (Roux et al., 2015) as the median of several cross-sections perpendicular to the flow, intersecting the active channel polygon and spaced 10 m.

Active channel width changes induced by the two floods (*Wr*, called "width ratio") were calculated as the ratio between the channel width after and the channel width before each flood (Krapesch et al., 2011):

$$Wr_I = W_{2017}/W_{2014} \quad (1)$$

$$Wr_{II} = W_{2020}/W_{2017} \quad (2)$$

where *W* is the average active channel width measured in 2014, 2017 and 2020.

Channel width evaluation, and consequently the width ratio, are affected by errors related to orthophoto interpretation and polygon digitalization, and overall, the absolute error is estimated to be in the order of 1–2 m.

Additional morphological parameters (Table 2) were assessed to characterize the morphology of each reach before and after the floods and to define their modification.

3.3.4. DEM of Differences (DoD): assessing changes in sediment storage

The assessment of elevation and sediment storage changes in the Stolla channel were accomplished using the difference of multi-temporal DTMs (Lane et al., 2003; Vericat et al., 2017). The DEM of difference (DoD) was obtained from the DTMs 2010 and 2017 for the event in 2017 and from the DTMs 2017 and 2020 to characterize erosion and deposition pattern related to the 2020 flood. Several studies (Lane et al., 2003; Lallias-Tacon et al., 2014; Schaffrath et al., 2015; Cavalli et al., 2017) have demonstrated that point clouds alignment may have a significant impact on sediment budgeting through DoD analysis (DEM of Difference). Therefore, before interpolation, the 2010 and the 2020 point clouds were aligned to the reference LiDAR point cloud of 2017, which is the most extended and accurate. The alignment of point clouds was performed using the CloudCompare software (https://www.danielgm.net/cc/).

DoDs were obtained using the Geomorphic Change Detection (GCD) software (http://gcd.riverscapes.xyz/) developed by Wheaton et al. (2010). The GCD software computes the volumetric and elevation changes in storage, from the difference in surface elevations from two DTMs and allows accounting for uncertainty. The FIS (Fuzzy Inference System) based methodology proposed by Wheaton et al. (2010), which permits to take into account spatially distributed DoD uncertainties (Brasington et al., 2000; Cavalli et al., 2008, 2017; Wheaton et al., 2010; Pellegrini et al., 2021) was used (for more details see section 1, supplementary material).

Because this study is mostly concerned with elevation and volumetric changes associated with debris flows in the tributaries and fluvial transport in the Stolla Creek, the DoD analysis was restricted to a mask including the Stolla river corridor after the floods and the debris flow processes mapped along the hillslopes, as in Minute et al. (2019).

Volumes of sediments eroded in the connected debris flows and toe erosion processes were computed (M_{df} and SS_{toe} in Table 2). However, uncertainties relative to such DoD results have to be considered. Specifically, mechanical removal by the Civil Protection Agency took place in some of the debris flow cones right after the event and DoD estimations do not include small sediment transport events (by snow avalanches, snowmelt runoff and minor rainfall events) that may have occurred between the two DTMs (Pellegrini et al., 2021). Because of the above uncertainties which does not allow us to precisely determine the sediment volume which actually entered the Stolla channel during event I, we used erosion volumes calculated at the sources areas to characterize and classify debris flow magnitude. In fact, coupled debris flows and toe erosion processes were classified into 3 classes, according to their magnitude (Jakob, 2005). In particular the debris flows classes include: Large ($M_{df} > 10{,}000$ m^3), Medium ($1000 < M_{df} < 10{,}000$), Small ($M_{df} < 1000$ m^3) magnitudes; while the toe erosions where classified as: Large ($SS_{toe} > 1000$ m^3), Medium ($500 < SS_{toe} < 1{,}000$), Small ($SS_{toe} < 500$ m^3) magnitude.

In river corridor, elevation changes were quantified considering the elevation difference of the two compared DTMs, as the main goal was to quantify elevation changes induced by the two floods, and to highlight areas of erosion and deposition. An attempt to discriminate whether channel widening occurred mainly by means of processes of channel lateral migration and erosion of the channel banks, or through overbank deposition of gravel and sand materials on the former floodplain was made. This analysis was not straightforward as the two processes may take place in different areas of the same channel reach – due to local morphological characteristics and to the stream power – or they can occur in the same reach section consecutively. For example, a portion of the floodplain may be firstly affected by channel lateral erosion, and then gravel deposition may take place. In this case, the widening is caused by bank erosion, but the subsequent sediment deposition can induce a positive net elevation change. For these reasons, in this study several indicators were integrated to classify the widening typology in each reach: the elevation changes in the channel areas that were part of the active channel after the flood but that constituted a floodplain before the flood (*AW*, area of widening, Table 2); the analysis of the evolution of the islands whether in new formation or erosion; and the preservation or erosion after the flood of trees rooted into the channel margins and the floodplain. In particular, where the DoD showed elevation raising associated with the preservation of trees and of pre-existing islands and the clear presence of gravel among the vegetation, main processes of overbank deposition (OD) were associated; on the contrary where the DoD showed elevation lowering, associated with vegetation and/or pre-existing islands removal or the formation of new dissection islands as the result of the fragmentation of the former floodplain, they were considered as a proxy of lateral erosion and bank erosion processes (BE).

Finally, a reach-scale computation of changes in sediment storage along the main Stolla channel was carried out using the sediment budget tool in the GCD software. The software estimates volumes of sediment eroded and deposited from the DoD by multiplying the calculated elevation change (a depth measurement in meters) by the surface area of each cell (1 m^2). Volumes were then summed into erosion or deposition categories to quantify net volumetric change at the reach scale. It is worth highlighting that the sediment storage analysis was carried out exclusively at the Stolla channel scale (quantification of sediments eroded and deposited at the output of each channel reach). This choice was due to the impossibility to obtain a sediment budget at the

catchment scale which requires the quantification of sediments released by the connected debris flows and the toe erosion processes to the Stolla channel. As said above, an unknown amount of sediments was removed especially from the main tributaries and from their fans by the local river managers, a few days after the flood in 2017 (and before the LiDAR survey). In addition, the analysis has highlighted some limitations in using topographic differencing from airborne LiDAR data to quantify debris-flow deposits with thickness of the same order of DoD uncertainty, leading to underestimating deposition volumes.

3.4. Statistical analysis of channel changes and environmental factors

Exploratory analyses of correlation among variables reported in Table 2 were performed using the Spearman's rank correlation, to understand statistical associations between the controlling factors for channel changes and to discern possible patterns in the relationship between channel modifications and potentially associated environmental factors.

Statistical significance of differences between groups of reaches affected by widening through bank erosion or overbank deposition was tested applying the non-parametric Mann-Whitney test. Statistical analyses were conducted within the statistical software R version 4.0.0 (R Development Core Team, 2020).

4. Results

4.1. Rainfall and flood response analysis

The 2017 event (event I) was caused by a rainstorm that started at 6:30 p.m. CET and lasted approximately 6 h, with a maximum rainfall intensity exceeding 45 mm/h. The cumulative rainfall depth during the event ranged from 40 to 84 mm over the Stolla catchment (Fig. 4A).

Cumulative precipitation exceeded 55 mm in the most of the Stolla basin; lower precipitations affected the eastern side of the catchment and the headwaters of the Prags Braies catchment. The return period is about 200 years for a rainfall duration of 1 h and decreases to 15 years for a rainfall duration of 24 h.

During this event, the peak discharge at the Prags River streamgauge reached 70 $m^3 s^{-1}$ (Fig. 4C). The rainfall-runoff model was calibrated on the hydrograph recorded at this flow gauging station; the calibration parameters were then transposed to the ungauged cross-sections where indirect peak discharge was estimated from the flood marks. The model-computed peak discharge for the Stolla catchment shows a moderate overestimation over the field-reconstructed value. The rainfall-runoff model was applied to assess the flow response at the 36 studied reaches in the Stolla: modelled peak discharges - range from 3.5 $m^3 s^{-1}$ at reach 1 to 63 $m^3 s^{-1}$ at reach 36. Total stream power varies between 4570 W m^{-1} at reach 1 and 80,100 W m^{-1} at reach 29, while unit stream power using pre-flood width ranges between 990 W m^{-2} at reach 15 and 18,500 W m^{-2} at reach 29.

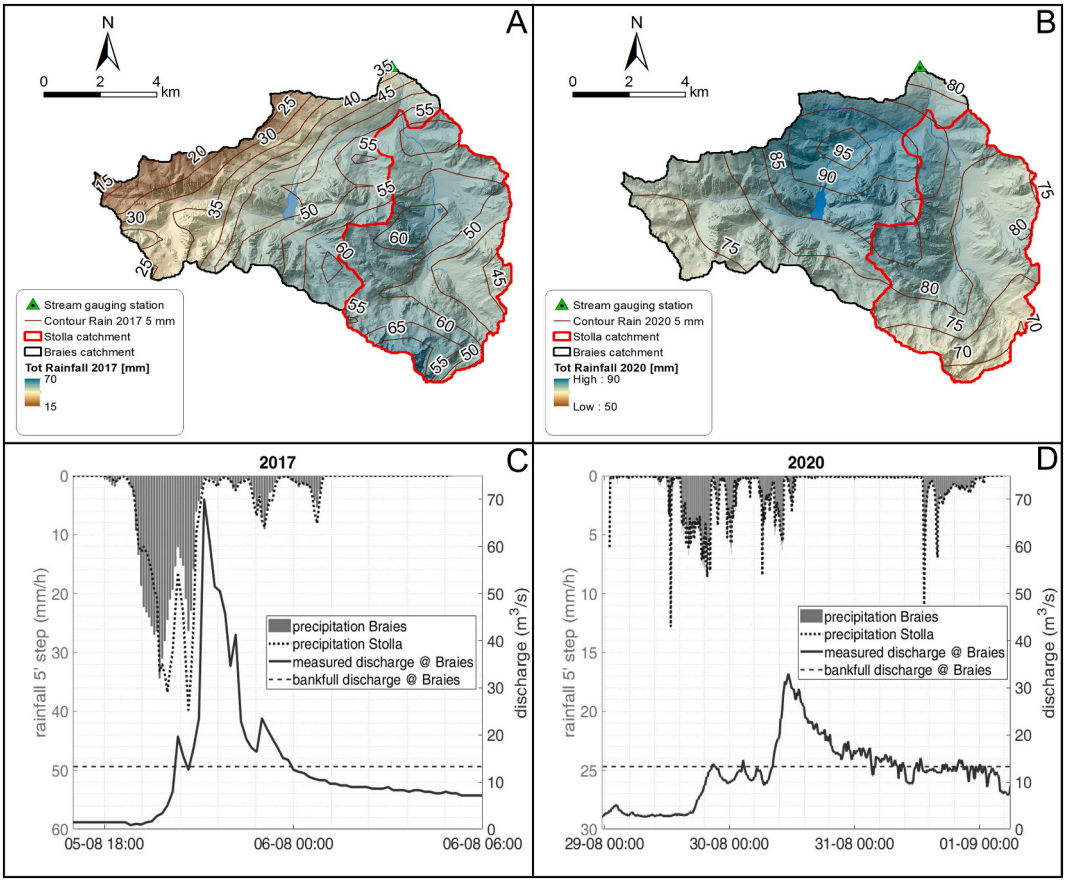

Fig. 4. Cumulative rainfall for 2017 (A) and 2020 events (B); recorded flood hydrograph at the Prags/Braies station for 2017 (C) and 2020 events (D). Recorded hydrographs are reported in solid black line together with average catchment rainfall for the whole basin (grey bar) and for the Stolla catchment (dotted line) for 2017 (C) and 2020 (D) events.
Severe intensities for 2017 event emerge considering rainfall and discharge magnitude (C) while total rainfall and much longer duration for the 2020 event can be inferred comparing isohyets and patterns in panels A and B along with C and D plot timescale difference. As a reference, bankfull discharge calculated for the Prags/Braies station is reported with a dashed line.

The 2020 flood event (event II) was caused by a rainstorm that started at 9:30 local time and lasted approximately 30 h, with a maximum rainfall intensity of 18 mm/h. The cumulative rainfall depth ranged from 64 to 102 mm over the Stolla catchment (Fig. 4B). The estimated return period is highest (15 years) for a rainfall duration of 24 h and decreases to 4 years for a duration of 1 h. For event II, the peak discharge at the Prags River gauging station reached 33 $m^3 s^{-1}$ (Fig. 4D).

4.2. Hillslope processes during event I

Six hundred and thirty debris flows were mapped in the Stolla catchment as activated during event I. They mostly originated from large talus slopes located at elevations between 2000 and 2400 m a.s.l., characterized by inclinations up to 45°. Debris flows initiated in concave-shaped terrains, with loose bare debris or sparse herbaceous vegetation. Most of them represented reactivations of debris flow already triggered in the past decades.

On the basis of field surveys and photointepretation, only 23 out of the 630 debris flows were classified as connected – i.e., with evidence of sediments supplied to the main Stolla channel - during event I (Figs. 3G, H, 1SA). High conditional frequencies of debris flows connected to the Stolla show that their activation occurred mainly in the following situations: i) elevations below 2200 m a.s.l. (Fig. 5A); ii) inclinations between 40° and 60° (Fig. 5B); iii) very small upstream catchments (mostly <0.15 km^2, Fig. 5C); iv) at a distance from the channel network <100 m (Fig. 5D); v) and where the wetness index indicates high wet conditions (Fig. 5E). Low frequency of connected debris flows was observed in sectors of the basin hit by cumulative rainfalls exceeding 53 mm (Fig. 5F).

Remarkably, the geomorphological characteristics along sediment pathways had a key control on the structural sediment disconnectivity to the main channel. In fact, most debris flows which initiated in the upper part of the basin (>2100–2200 m a.s.l.) stopped at hanging valleys or on high altitude talus slopes or on debris cones (Fig. 6A).

Those debris flows that were able to reach the Stolla valley stopped on their fans (mainly at superimposed fans sensu Bull, 1968; see also Santangelo et al., 2012) or on alluvial plains (Figs. 6B, 1SB). Sediment deposition during event I reached up to 7 m on some debris-flow fans (Fig. 6B). Connected debris flow developed along both the left and right side of the Stolla valley. On right valley side, debris flows originated and moved in entrenched fan systems (sensu Bull, 1968; see also Santangelo et al., 2012). These fans are quite large with areas ranging between 0.1 and 0.7 km^2 and lengths between 1000 and 1400 m. Despite the occurrence of deposition, part of the debris flow sediments were able to reach the Stolla channel. Connected debris flows on the left valley side developed on coalescing fan systems (Fig. 6D). Compared to the fans on the right side, these debris fans are smaller (total area ranging between 0.01 and 0.7 km^2), and shorter (fan length ranging between 150 and 800 m).

Remarkably, debris flows classified as connected - through photo-interpretation and field observation - present IC values (Cavalli et al., 2013) significantly higher (p-value < 0.05) than those classified as disconnected (Fig. 7A, B).

Sediment supply volumes associated to connected debris flows span a wide range, reaching a maximum value of about 74,100 m^3 at those entering in reach 11. Overall, small magnitude debris flows resulted to be more connected to the main channel (median values > −2.5, Fig. 7C); medium and larger debris flows presented a wider range of index of connectivity width median values attaining values < −2 (Fig. 7C). Toe erosion processes affected most reaches with sediment supply up to about 4500 m^3 (reach 29).

Differently from event I, no debris flows were triggered by event II, and only some toe erosion processes were observed.

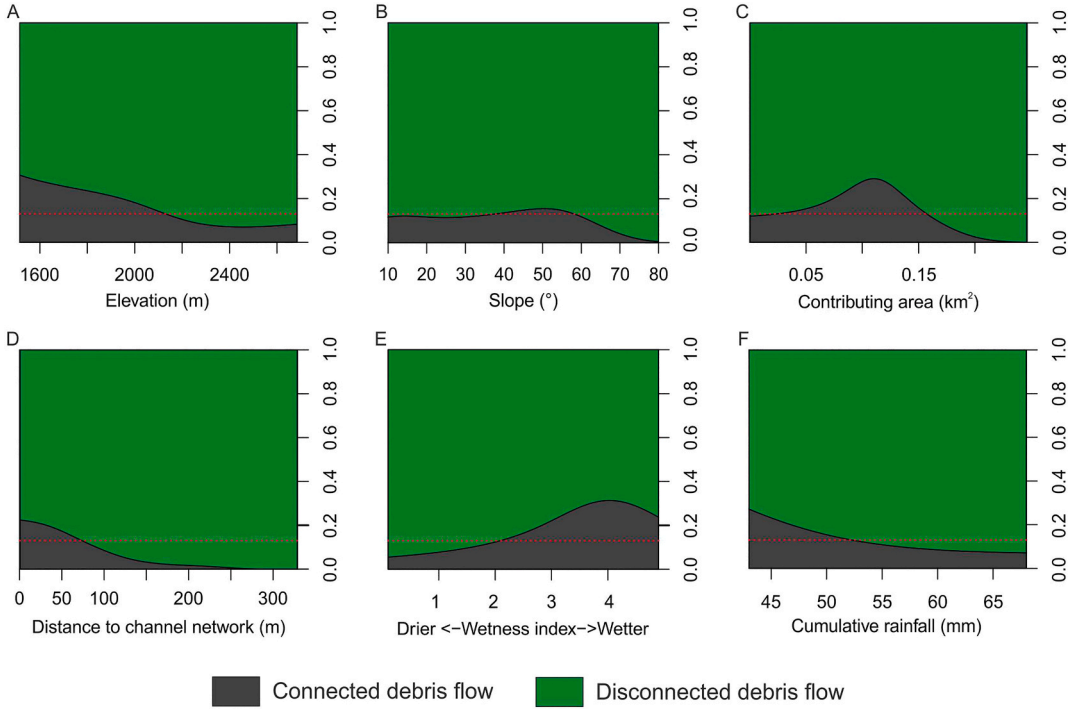

Fig. 5. Conditional frequency illustrating the ratio of connected debris flows and disconnected debris flows for some variables evaluated at the debris flow releasing areas: elevation (A); slope (B); contributing area (C); distance to the channel network (D); topographic wetness index (TWI) (E); cumulative rainfall (F). The dashed red line separates areas with an over-proportional occurrence of connected debris flow observations (dark areas above the threshold) from areas associated with an over-proportional occurrence of disconnected debris flows (dark areas below the threshold). (For interpretation of the references to colour in this figure legend, the reader is referred to the web version of this article.)

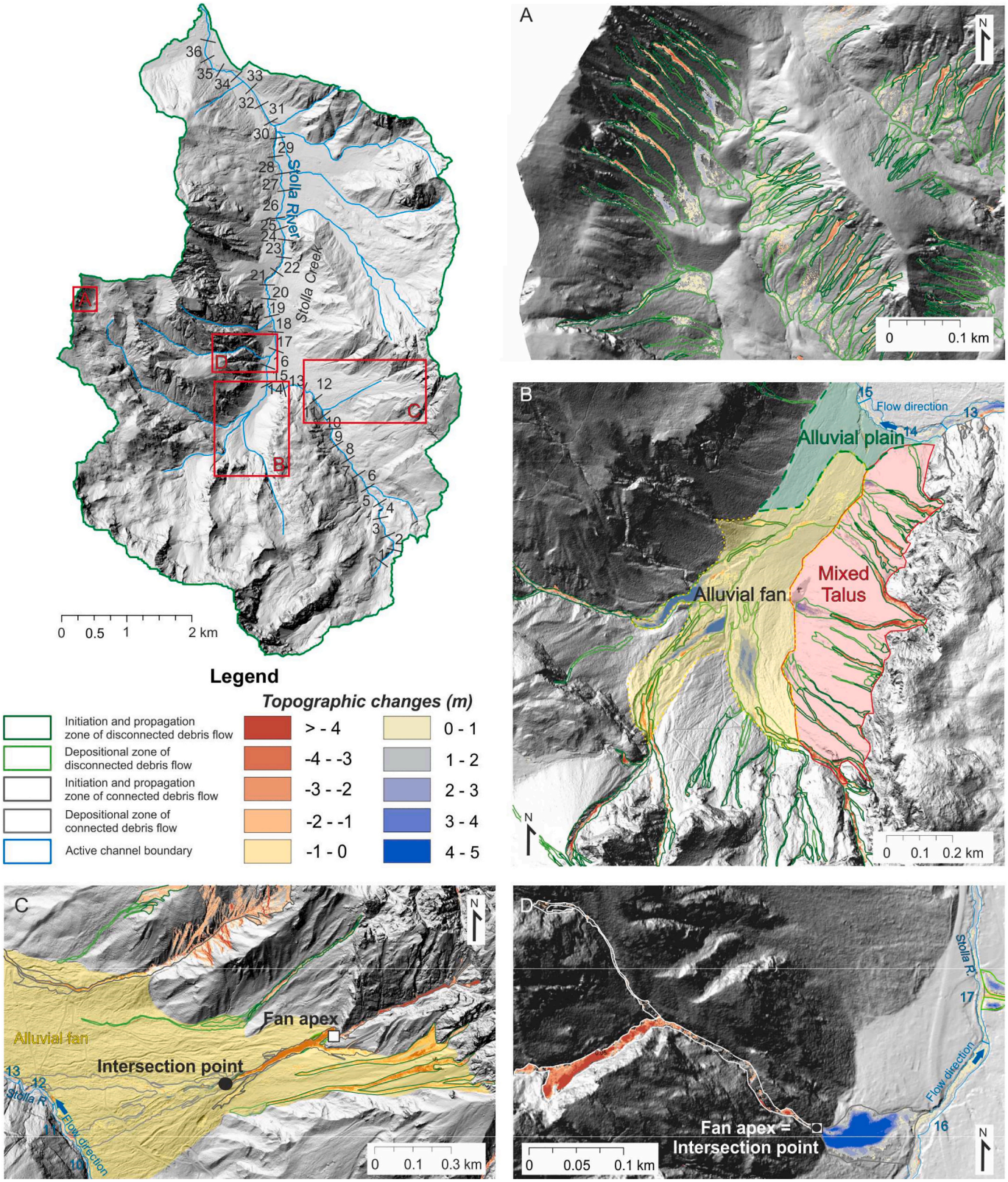

Fig. 6. Example of connected and disconnected debris flows in the Stolla catchment. Disconnected debris flows (A); debris flows disconnected by the talus, alluvial fans and alluvial plain (B); connected debris flows (C, D).

4.3. Channel changes induced by events I and II

The two flood events induced morphological changes of different magnitude in the Stolla valley floor. Event I caused remarkable planform changes consisting in channel widening, pattern changes, channel lateral migrations, islands formation or erosion and valley confinement modifications. The average channel width before the flood ranged between 2 m and 17 m (Fig. 8A) whereas after the flood from 4 to 27 m

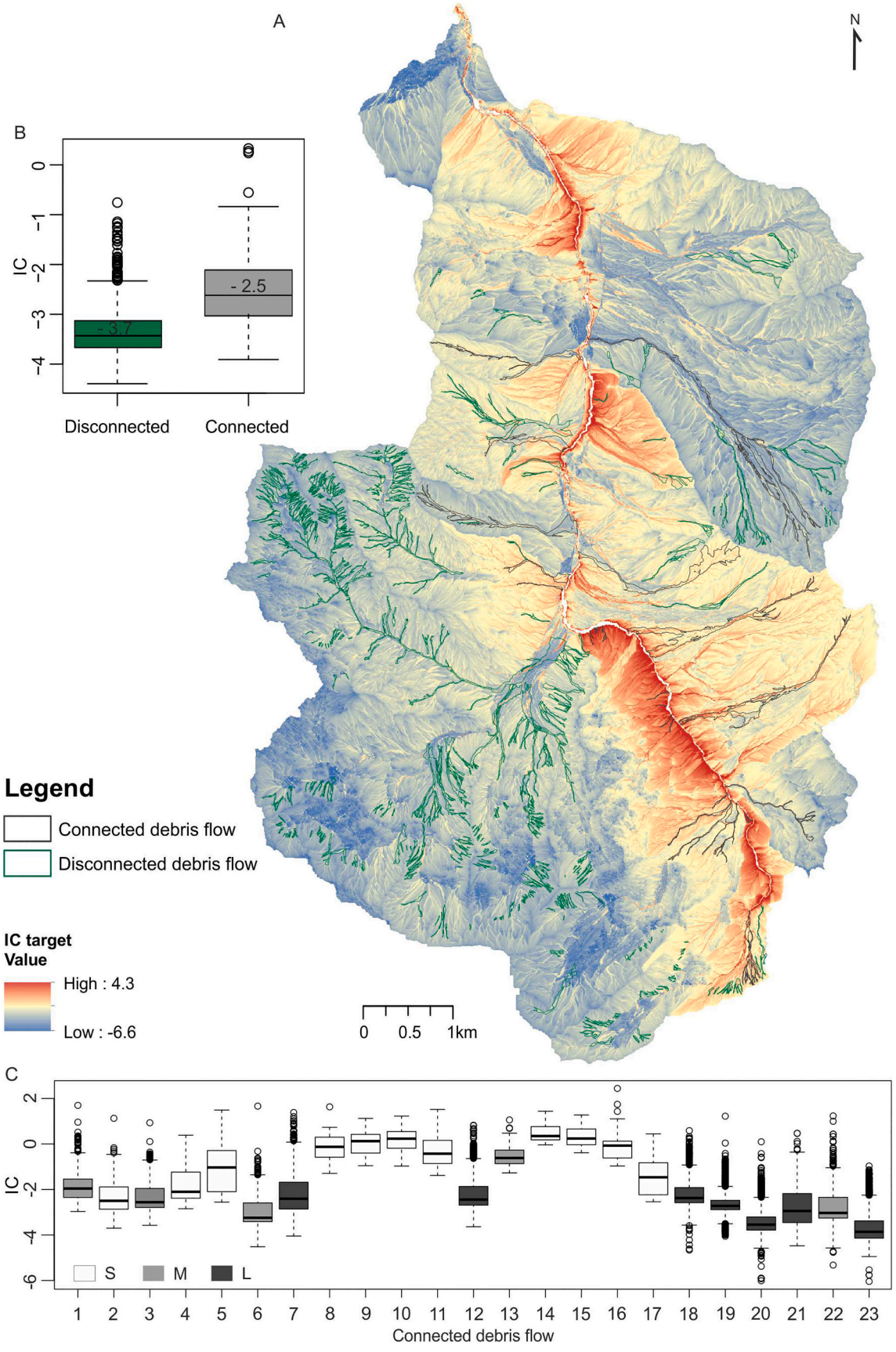

Fig. 7. Map of index of connectivity using the Stolla as target (A). Box and whiskers plots presenting median and interquartile range (25th and 75th percentiles), of the connected and disconnected debris flow with respect to the Stolla channel (B); of the IC distribution in the connected debris flows (C). Debris flows magnitude classes: S < 1000 m^3; 1000 m^3 < M < 10,000 m^3; L > 10,000 m^3.

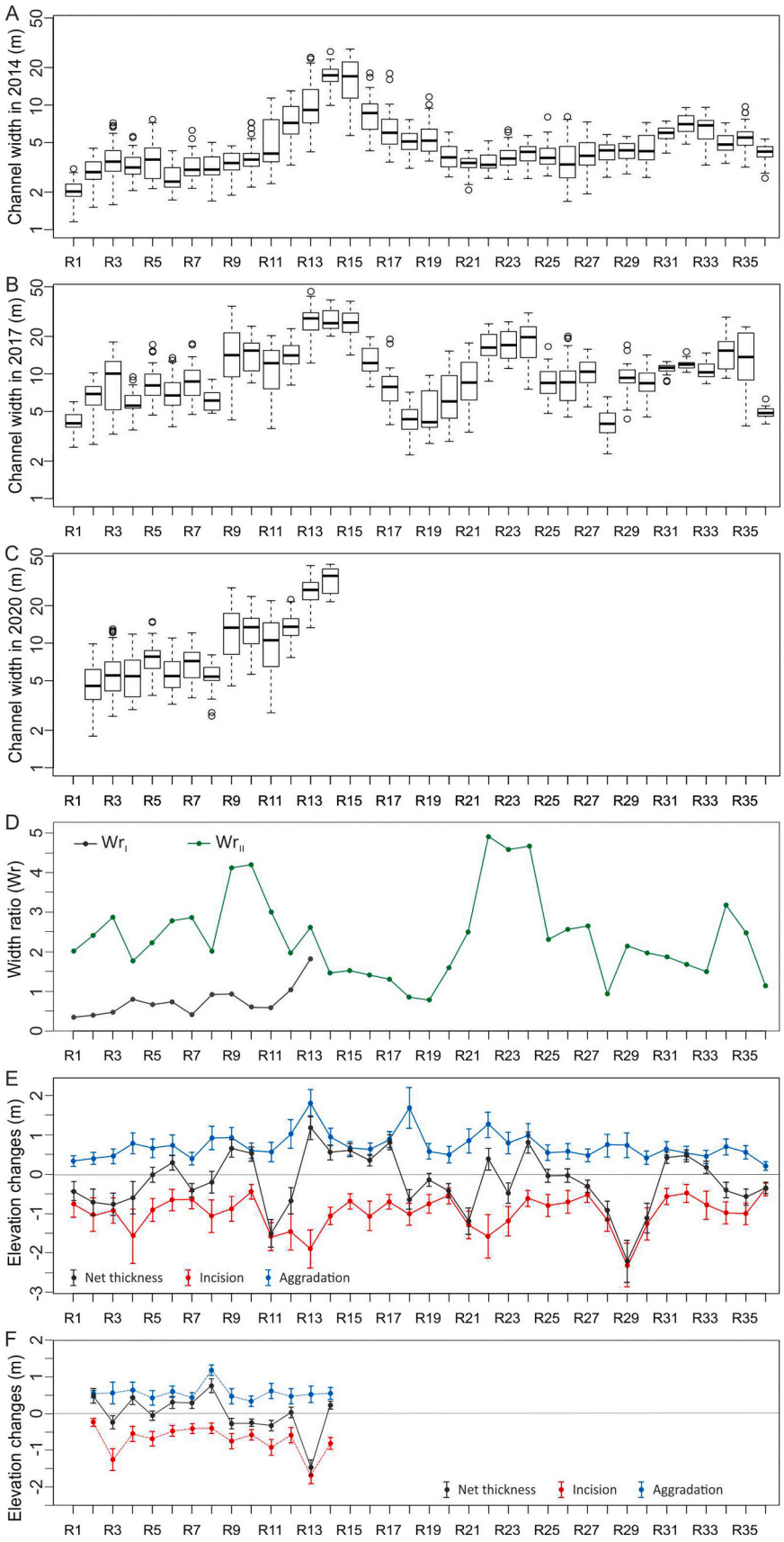

Fig. 8. Box and whiskers plots presenting median and interquartile range (25th and 75th percentiles) in the studied reaches of: channel width in 2014 (before event I, A); channel width in 2017 (after event I, B); channel width in 2020 (after event II, C); median values of width ratio for event I (Wr_I) and II (Wr_{II}, D); elevation changes in the river corridor between 2014 and 2017 (due to event I, E); elevation changes in the river corridor between 2017 and 2020 (due to event II, E).

(Fig. 8B).

Channel width after event I was up to 5 times larger than before, and on average 2 times wider in most reaches (Fig. 8D). Channel widening occurred by both bank erosion and overbank deposition (see also Section 4.5). Channel widening was associated with pattern changes (Fig. 2SA, B, supplementary material): before the flood, 22 reaches presented a sinuous and 14 reaches a straight planform morphology, after the flood most reaches shifted to a sinuous with alternated bars pattern (20 out of the 36), 5 reaches presented a sinuous pattern and 11 maintained the straight morphology. Channel sinuosity decreased in all reaches. Channel lateral migration was quite uniform, in the order of a couple of meters; noteworthy was the avulsion that occurred in reach 18, where a debris fan entering the valley bottom pushed the channel toward the opposite side of the valley (Fig. 1SA). New dissection islands (area between 16 m^2 and 1495 m^2), as the result of the fragmentation of the former floodplain, were created in 12 out of 36 reaches; pre-existing islands were completely eroded in 6 reaches (Fig. 2SC, D, supplementary material). In the reaches from 30 to 33, former islands located between two consecutive grade-control structures were completely removed by the flood (Fig. 2SE, F, supplementary material). During the 2017 event, average floodplain width decreased by about 40%.

In sharp contrast, event II brought about limited planform changes: the average width remained quite similar to that measured after the 2017 event (Fig. 8D, $p\text{-value}_{W2017\text{–}W2020} = 0.31$), with a width ratio between 0.9 and 1 (Fig. 8C).

Elevation changes in the river corridor caused by event I - assessed through the 2014–2017 DoD analysis - indicates that all reaches experienced both incision and deposition (Fig. 8E).

However, a net incision prevailed in most reaches (24 out of 36), achieving maximum reach-averaged values (−2.2 m) at reach 29 (Fig. 8E). Maximum local incision also peaked (−4.5 m) in reach 29 (Fig. 9). In the reaches that experienced net deposition, average deposition thickness ranged between 0.30 m (reach 6) and 1.2 m (reach 13), (Fig. 8E), and maximum local aggradation attained 4 m in reach 13 (Fig. 10A).

As to event II, net average elevation changes in the river corridor ranged between 0.76 m in reach 8 and −1.45 m in reach 13, but in most reaches it was approximately ±0.40 m (Fig. 8F). In contrast to event I, during event II reach 13 underwent incision (Fig. 10B), i.e. the flood flows eroded sediments deposited during event I (Fig. 10A).

4.4. Longitudinal sediment transfer during events I and II

Fig. 11A shows the distribution and magnitude of sediment supply from connected debris flows and toe erosions during event I (see Section 4.2).

Longitudinal sediment storage variations along the Stolla channel – derived from the 2010–2017 DoD – confirms that alternated processes of erosion and deposition occurred during event I (Fig. 11B). In fact, reaches from 1 to 12 – except for reach 9 and 10 – were characterized by slightly negative net changes (i.e., sediments volume exiting the reach greater than the volume entering the same reach). In contrast, reaches from 13 to 17 – highly affected by lateral sediment supply – show a marked net deposition (up to 6500 m^3 at reach 13). Overall, the total sediment volume eroded from reaches 1 to 12 (approximately 3170 m^3) is much lower than the total deposition volume in the reaches from 13 to 17 (approx. 13,210 m^3), and therefore the cumulative storage variation - computed as the cumulative difference of absolute values of erosion and deposition - becomes highly negative (i.e., strong prevalence of net deposition) at reach 17.

Downstream, from reach 18 to the outlet, channel reaches show an alternation of slight positive and negative changes in sediment storage, with the exception of reach 29 characterized by a large negative value (i.e., net erosion) which reduces the negative cumulative changes. Finally, in the reaches from 31 to 33 net sediments deposition was very likely favored by the presence of check dams, as new medial bars formed

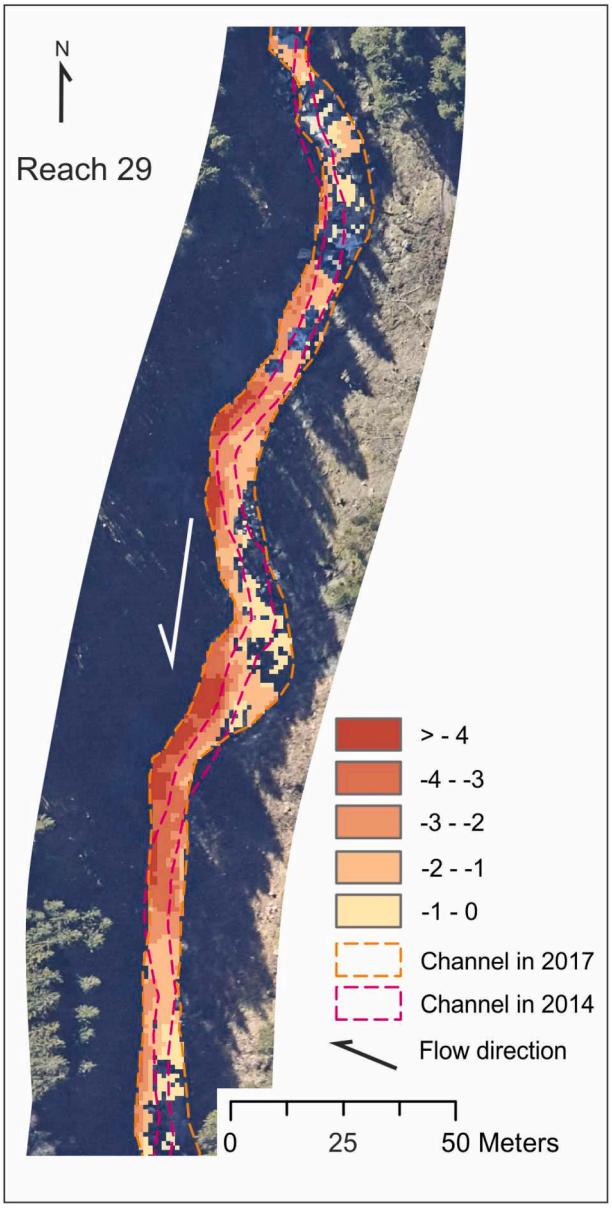

Fig. 9. Elevation changes distribution in the river corridor at reach 29 between 2010 and 2017.

downstream of each structure during event I (Fig. 11B).

Overall, the cumulative storage variations occurred during event I turn out to be negative at the Stolla basin outlet (−934 m^3, Fig. 11B), which highlights a prevalence of sediment deposition over erosion along the whole valley floor. This result, when coupled to field observations carried out immediately after the event I that showed absence of deposition at the Stolla-Prags rivers confluence, negligible bedload transport in the Prags River downstream as well as negligible deposition at the Prags-Rienz rivers confluence, suggest that coarse sediments volumes exported from the Stolla to the Prags River during this extreme event must have been quite small, especially when compared to the large amount of sediment mobilized at the catchment scale.

Longitudinal sediment transfer during event II along the upper Stolla segment (reach 2 to 14, the only channel length which was resurveyed by laser scanning) was very different from event I. In fact, changes in sediment storage derived from the 2017–2020 DoD (Fig. 11C) indicate an opposite dynamics compared to event I, as most reaches from 2 to 8 exhibit positive changes (i.e., net deposition) and reaches 9, 10 and 13

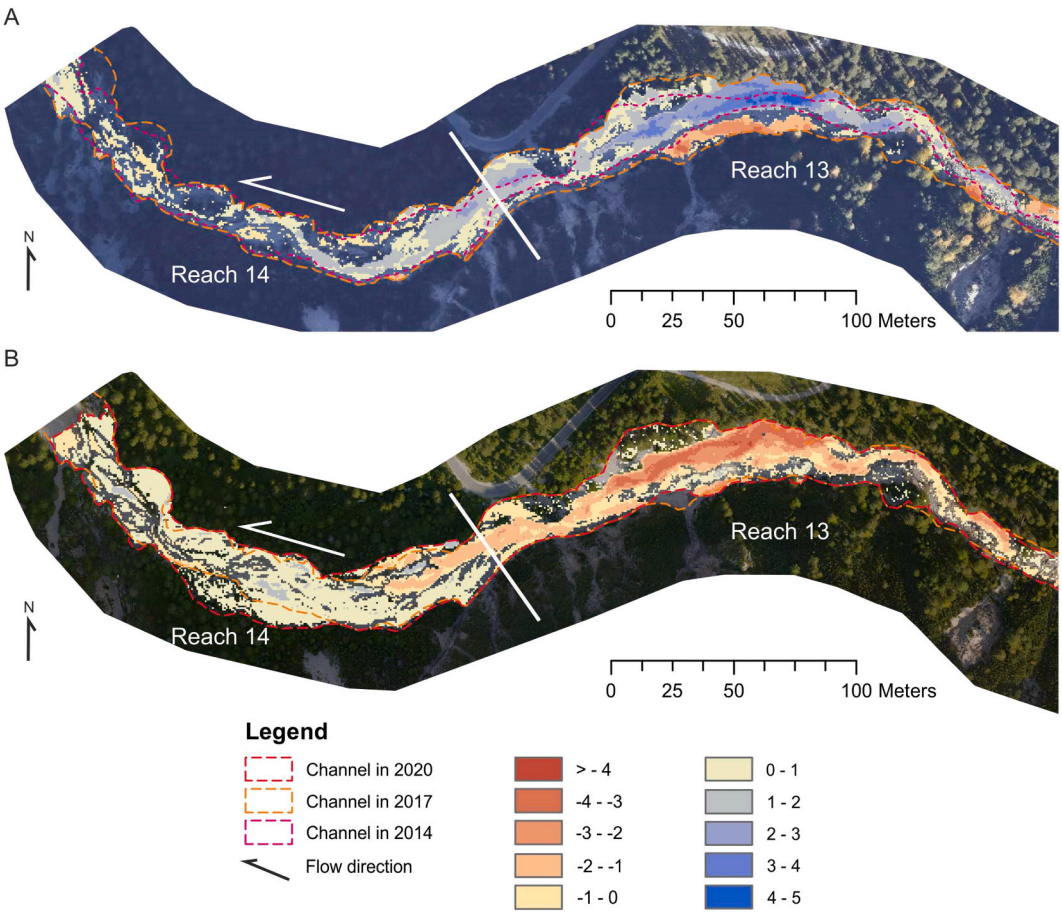

Fig. 10. Elevation changes distribution in the river corridor at reaches 13 and 14 between 2010 and 2017 (event I, A) and between 2017 and 2020 (event II, B).

net erosion during event II, nicely contrasting with what observed during event I in the same reaches. Field observations after event II also suggest that most of sediment volume exported from reach 13 (about 7000 m^3) was deposited in the reach immediately downstream, and no further depositional or erosional processes were observed downstream of the confluence with the Prags River.

4.5. Factors controlling channel changes during event I

Fig. 12A shows the Spearman correlation matrix among all analyzed morphometric, geomorphological and hydraulic variables (Table 2). Noteworthy are the positive correlations between the channel slope (*Sp*) and the confinement degree (*Cd*), as stepper channels have high longitudinal confinement. In contrast, channel slope presents negative correlations with peak discharge (Q_{pk}), sinuosity index (*SI*) and with a set of parameters describing the possibility of the channel to migrate laterally such as the confinement index (*CI*) and channel lateral migration (*LatMig*, $LatMig_{max}$). Reaches that experienced higher lateral migration are in wider valley sections (positive correlation between *LatMig*, $LatMig_{max}$ and *CI*) and were affected by higher peak discharge (positive correlation between *LatMig*, $LatMig_{max}$ and Q_{pk}). Toe erosion processes (SS_{toe}) show a high correlation with unit stream power (ω).

Elevetation changes in the river corridor (ΔH) are positively correlated with channel width before the flood (W_{pre}) and negatively correlated with unit stream power (ω) and occurrence of toe erosion processes (SS_{toe}). Aggradation in the river corridor (ΔH_{aggr}) is positively correlated with channel width and lateral migration. Incision is favored in steeper reaches, more confined by hillslopes (negative correlation with *Cd*), in reaches with lower sediment supply from toe erosion (negative correlation with SS_{toe}) and affected by higher unit stream power (ω). The width ratio (*Wr*) shows significant negative correlations with the confinement before the flood (*Cd*) and a positive correlation with the confinement index (*CI*), which not surprisingly indicates that strongly confined channels tend to undergo less relevant widening. Moreover, widening was more intense in the channels which were narrower prior to the flood event (negative correlation between *Wr* and W_{pre}). Finally, it is worth to highlight the very poor correlation between channel width changes (*Wr*) and elevation changes in the river corridor (ΔH, ΔH_{inc}, ΔH_{aggr}, Figs. 12A and 3S).

The results show how different types of processes for channel widening take place depending mostly on valley confinement, valley slope and channel width. In fact, widening by means of processes of bank erosion were more common in narrower reaches (Fig. 12B, C), more confined (Fig. 12D), and affected by higher stream power due to steeper gradients (Fig. 12E). These reaches exhibited more intense incision (Fig. 12F), while opposite characteristics was are featured by the reaches where widening occurred mostly through overbank deposition.

5. Discussion

5.1. Contrasting geomorphic effects of different storm events

The quantitative comparison of the geomorphic effects associated to the 2017 (event I) and 2020 (event II) floods in the Stolla channel provides novel insights about the role of flood characteristics upon the associated morphological changes in confined/partly confined and steep mountain channels.

The 2017 event was a flash flood with very high rainfall intensities (up to 45 mm/h), in the order of 200 years in terms of recurrence

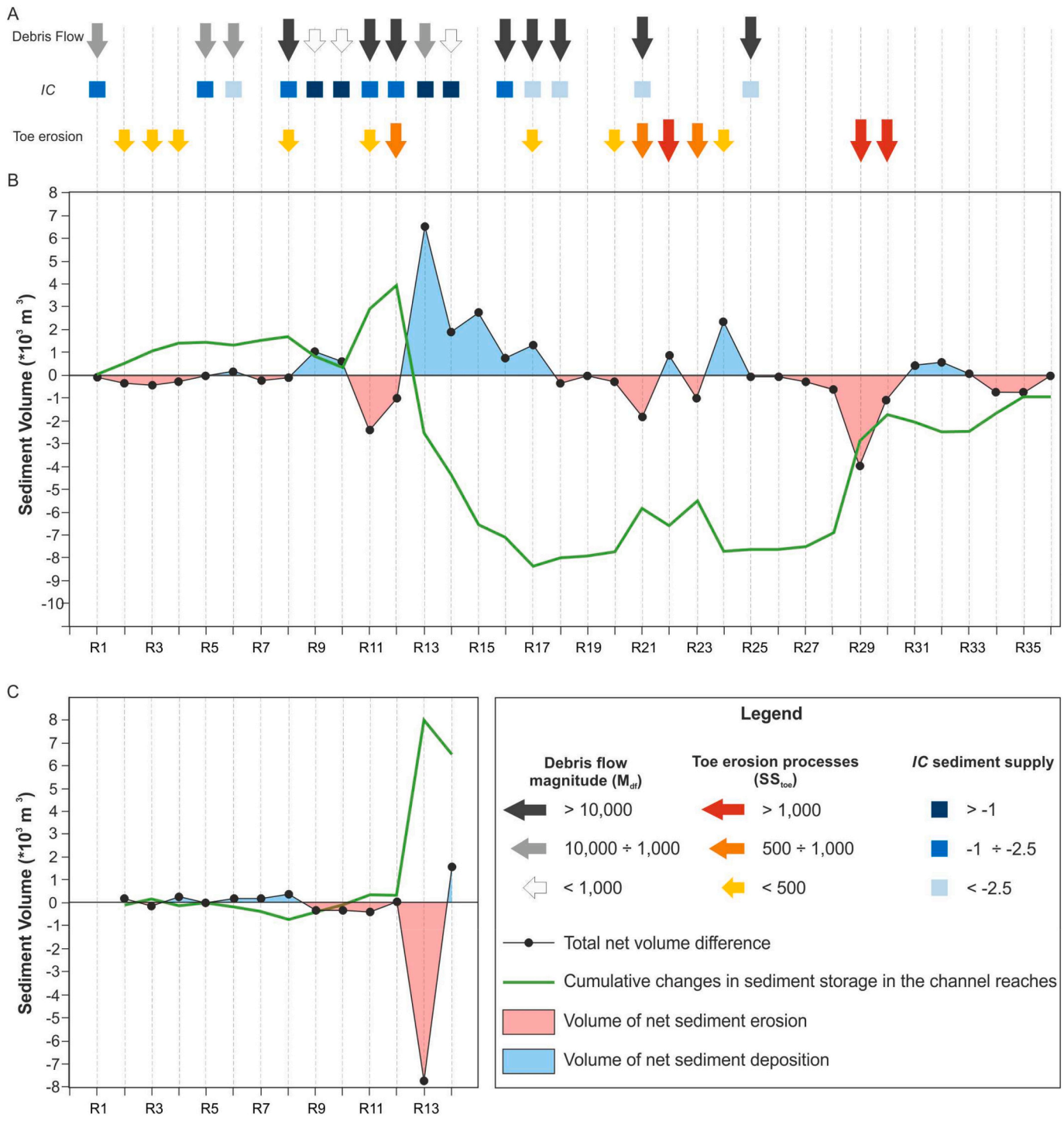

Fig. 11. Longitudinal distribution and magnitude of sediment supply from debris flows and toe erosions during event I (August 2017, A); net and cumulative sediment storage changes in the Stolla channel due to event I (B), and event II (August 2020, C). Cumulative sediment storage change has been computed as the cumulative difference of absolute values of erosion and deposition.

interval for storm duration of 1 h. During this event, the Stolla channel received a substantial input of sediment from debris flows.

Unfortunately, we could not quantify precisely the sediment volumes that reached the main channel but only the debris flow volumes entrained upslope: we can estimate that about 294,000 m^3 of sediments were eroded in the connected debris flows. In addition, fluvial-induced toe erosions contributed to about 12,400 m^3. Despite the very high unit stream power associated to the flood peak (between 990 W m^{-2} and 18,500 W m^{-2}), a balanced alternation of incised and aggraded reaches could be inferred from the DoD results, with important channel widening occurring in both cases. Remarkably, combining field observations carried out right after event I – both by the authors and by local river managers (Civil Protection Agency of South Tyrol, personal communication) – with the cumulative variations in sediment storage (Fig. 11), allow us to affirm that sediment volume exported from the Stolla channel during this event must have been very small, in the order of few thousands of m^3 at most. The very short duration (6 h) of the 2017 storm and consequent flashy hydrograph (Fig. 4C) are the most likely

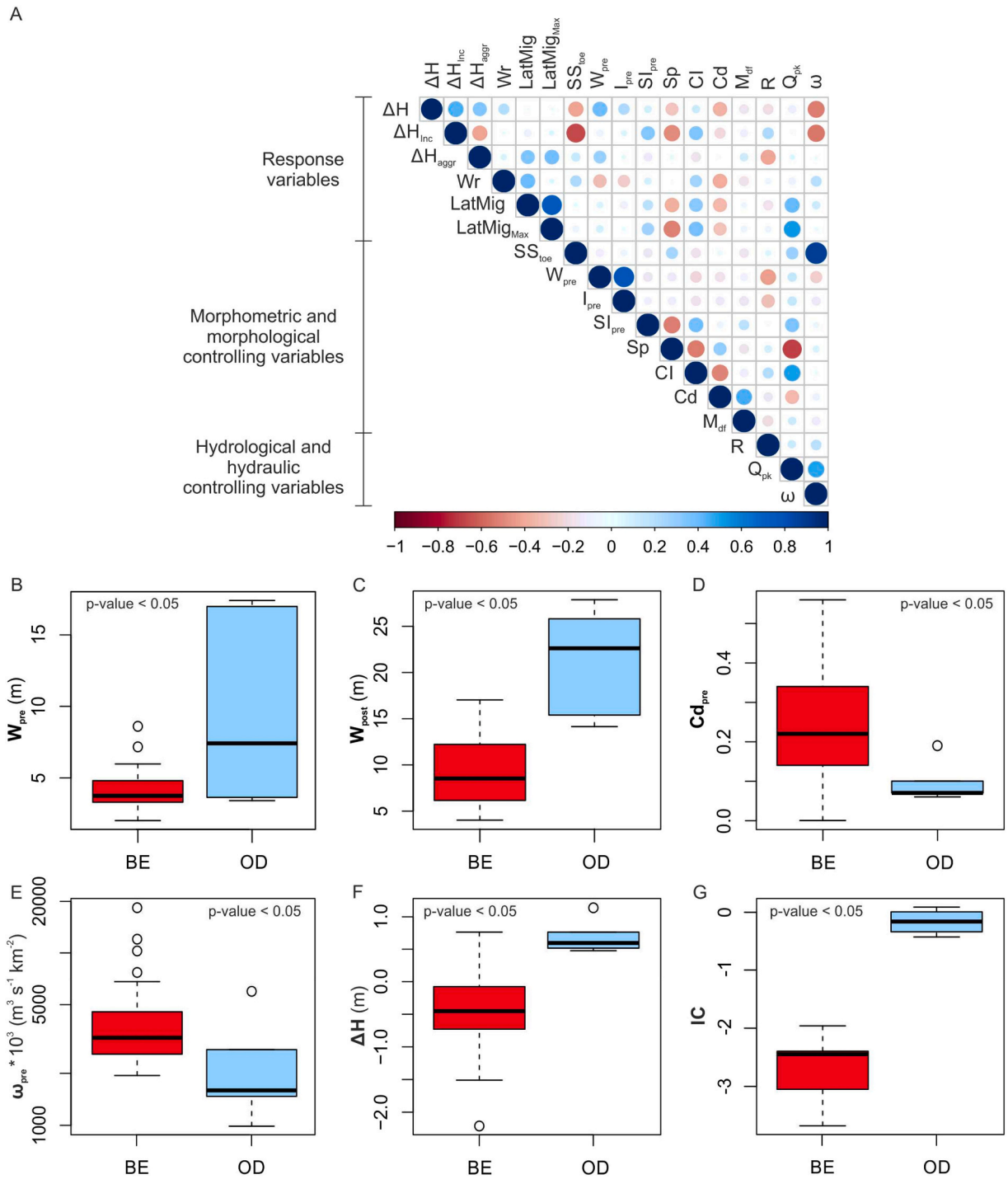

Fig. 12. Spearman correlation matrix of all analyzed variables for all reaches. Red and blue colours show negative and positive correlation, respectively, white colour shows not significant correlation (p-value > 0.05). The bar under the matrix show the Spearman rank value (A); box and whiskers plots presenting median and interquartile range (25th and 75th percentiles) of the reaches widened by means of processes of bank erosion (BE) and of overbank deposition (OD) with respect to: channel width before the flood (B); channel width after the flood (C); confinement degree (D); unit stream power using pre-flood width (E); elevation modification in river corridor (F); index of connectivity (G). For codes see Table 2. (For interpretation of the references to colour in this figure legend, the reader is referred to the web version of this article.)

reasons for such a short transport effectiveness of the event, which translates into a poor functional longitudinal connectivity of sediments fluxes during such as flashy event. Short alternations of bed incision and aggradation – without a clear, monotonic longitudinal pattern – seem to confirm that coarse sediment transport has had not enough time to take place along the whole Stolla channel, preventing a redistribution from the local sediment input sites associated to debris flows and toe erosion. Therefore, the 2017 event represents a paradigmatic case of strong hillslope-channel coupling – although limited to a small percentage of the active debris flows – with large volumes of sediment supply of colluvial origin leading to profound morphological variations in the whole river corridor, i.e., both in the channel and in the small floodplains where present. A similar case of large flood – occurred in 1994 – featuring "unlimited supply conditions" and major channel changes has

been well described in the Rio Cordon (Lenzi, 2001; Lenzi et al., 2004), a smaller (5 km^2) mountain channel in the Dolomites for which almost 30 yr of channel morphology and sediment transport monitoring is available (Rainato et al., 2018). In that case, most of the coarse sediment supply originated from the channel bed and banks, with limited amounts from the hillslopes. Nonetheless, both the 1994 flood in the Rio Cordon and the 2017 flood in the Stolla Creek can be reasonably assumed to have been transport-limited because of their short duration, as observed also for other extraordinary (recurrence intervals $>$ 50–70 yr) events (Turowski et al., 2009; Rickenmann and Koschni, 2010; Comiti and Mao, 2012; Rickenmann et al., 2016).

Totally different is the case of the 2020 flood event (event II). This event featured cumulative precipitation greater than for event I, but its temporal evolution and maximum rainfall intensities contrast sharply with the latter one, and overall the recurrence interval of the storm is in the order of 4 years (for a rain duration of 1 h). Such lower rainfall intensities were not able to trigger significant debris flows in the study catchment, i.e., this storm was not able to functionally connect the structurally connected hillslopes and tributaries. During event II, flood peaks in the main channels resulted about half of those observed in 2017. Nonetheless, the high cumulative precipitation determined an important flood runoff volume, which has been geomorphically quite effective in terms of channel change (bed incision) in those reaches where aggradation – mostly gravel and small cobbles – occurred during event I. However, the moderate magnitude of the flood peak did not lead to lateral erosion, with the exception of local deposits left by the 2017 event. Therefore, the 2020 event represents an example of ordinary, moderate flood during which the hillslope-channel coupling cannot take place because of the relatively low rainfall intensities unable to destabilize hillslopes and colluvial channels. Consequently, such events in steep mountain channels are supply-limited (Montgomery and Buffington, 1997) and thereby with a tendency to incise the bed provided the substrate is mobile enough to be entrained. Indeed, the in-channel deposits left by the 2017 event in the Stolla were very likely still very loose and poorly armoured in 2020 – due to the short duration of competent flows between the two events – when a rather ordinary flood resulted competent to mobilize a significant amount of bedload with important geomorphic changes in some reaches. We can again draw an example with the Rio Cordon, where measured bedload volumes in the years immediately following the flood were relatively – in relation to effective runoff volume – much higher than before that large event. Also, a waning phase in bedload volumes lasting about a decade was evident in the Rio Cordon, as mobile sediments were progressively eroded from the channel, with bed armoring and pool depth increasing over time (Lenzi et al., 2004; Rainato et al., 2021). Similar temporal dynamics can be envisaged for the Stolla Creek, where a progressive self-stabilization of the channel bed is likely going to occur over the next years, with reduced bedload volumes and channel changes, until the next intense storm able to couple to hillslopes and channel will occur.

5.2. Landscape connectivity: structural and functional connectivity of sediment cascades

This study confirms that sediment movement in a catchment is mainly related to episodic pulses (Benda and Dunne, 1997; Fryirs et al., 2013). In light of this, the comparison of the two flood events in 2017 and 2020 has shown that the degree of sediment flux connection or disconnection can depend on floods magnitude, duration and frequency but also on the catchment morphology implying the presence and spatial distribution of landforms able to disconnect portions of the catchment. Furthermore, it is worth noting that the results of sediment connectivity analysis seem to suggest the prevalent role of structural connectivity (sensu Bracken et al., 2015a, 2015b) on sediment delivery to the Stolla channel network during the high-intensity rainfall event in 2017. On that event, connected areas were not affected by the highest amount of rainfall (Figs. 4A, 5F) but they were responsible for most of the sediment supply to the main channel (Upper-Eastern portion of the basin, Fig. 7). Conversely, as already stressed before, the intense rainfall that hit the western portion of the catchment caused the activation of several sediment source areas triggering debris flow processes but the sediment mobilized in this area did not reach the Stolla channel due to the decoupling effect of the large and gentle slope of the tributary valley floor that limited transport capacity. Several authors highlighted the importance of landscape structure and its variations for sediment connectivity and dynamics (Cossart et al., 2018; Cossart and Fressard, 2017; Cucchiaro et al., 2019; Llena et al., 2019). Conversely, Baartman et al. (2020) observed that all the models applied suggested that functional aspects of connectivity were more important than structural one. As also stated by the same authors, the catchment complexity may play a role in explaining the lack of relation between external forcing as rainfall and catchment response. This is the case of mountain catchments, where topographic configuration and the sequence of landforms are important factors controlling sediment connectivity. In 2017, in the Stolla catchment, the main role in interrupting sediment cascade was played by hanging valleys and talus and debris cones. Referring to the concept of effective catchment area (ECA) by Fryirs et al. (2007), it is possible to assert that in 2017, ECA reached a large value, as talus slopes, and most of the alluvial/debris fans did not act as buffers (Fryirs et al., 2007), actually, they were the primary sources of sediment able to reach the main channel. Most portions of the catchment classified in the higher range of structural sediment connectivity supplied sediment to the main channel (Fig. 7A). During the flood in 2020, only longitudinal connectivity in the Stolla was activated, driven by sediment transport in the channel, and the overall effective catchment area to the sediment cascade was limited to the valley bottom. Despite the massive activation of numerous sediment sources in the hillslopes in 2017, available sediment was still far from being exhausted in 2020, as unlimited sediment storages are present in the talus slopes (Figs. 6 and 1S). These important storages could have supplied sediment also in the case of the event in 2020. We argue that an important role in the different sediment delivery between the two events has been played also by functional connectivity (sensu Bracken et al., 2013) since intensity and duration of rainfall were quite different for the two events.

Findings from this study also confirm that the analysis of the sediment connectivity, both structural and functional, can help to interpret the different catchment responses to the two floods. As already mentioned in Section 5.1, the high intensity rainfall in 2017 was responsible for the triggering of debris flows but, because of its short duration, the sediment sources contributing to the channel network were limited to the areas more closely connected. As observed by Reid et al. (2007), lower intensity and longer duration storms may prove more effective in delivering sediment. The situation could be different over longer timescales when moderate-sized events that, according to Reid et al. (2007), deliver the majority of sediment inputs to the main stream, are likely to occur.

Finally findings showing that only a minimum fraction of the sediment eroded in the Stolla catchment has made its way to the outlet confirm that the sediment cascading between nested catchments or even between different zones within a catchment is very slow, as it progresses along topological sequences of neighboring storage compartments (Walling, 1983; Fryirs et al., 2007). In general, it is possible to assert that sediment spends considerably longer time in storage than in transport during sporadic remobilizations related to extreme floods affecting wide areas (Otto et al., 2009; Fryirs et al., 2013).

5.3. Factors controlling morphological changes during floods

Channel widening caused by the extreme event in 2017 is comparable with those reported by other studies at the European level, as width ratios are in the same range (average values between 0.8 and 4.9) to those observed for other large floods (between 1.17 and 5.5; Krapesch et al., 2011; Surian et al., 2016; Rinaldi et al., 2016; Righini et al., 2017;

Lucía et al., 2018; Ruiz-Villanueva et al., 2018; Scorpio et al., 2018).

New findings from this study indicate that the types of processes for channel widening – through bank erosions or overbank deposition – may reflect different characteristics of the valley confinement, of the channel geometry and of the flow energy. This can provide some important insights for river corridors management, as the expected geomorphic impacts can vary on the basis of the morphologic and morphometric characteristics of the valley bottoms. In fact, this study has found that widening by means of processes of bank erosions occurred mainly in narrow, steep and more confined reaches affected by higher flow power. These channels suffered an overall valley bottom degradation consisting in bed level lowering, floodplain and islands stripping, bank collapses and toe erosions processes with the consequent delivering of additional large wood. Reaches prone to widening through over bank deposition presented less confined valley configurations and relative wider channels before and after the flood. They experienced a more consistent aggradation in the bed on the floodplains and on the islands.

In agreement with other researches (Heritage et al., 2004; Thompson and Croke, 2013; Surian et al., 2016; Righini et al., 2017; Ruiz-Villanueva et al., 2018; Scorpio et al., 2018), this study confirms the role of the flood power and of the valley confinement in driving the channel adjustments.

Equations for confined and unconfided reaches (based on confinement index and unit stream power using pre-flood channel width) proposed by Scorpio et al. (2018) for a northern Apennine catchment composed of sedimentary rocks, especially sandstones and mudstones, were applied to the Stolla. For most reaches, predicted width ratios are slightly higher than the measured values in this study (measured Wr ranging between 0.8 and 5; predicted Wr ranging between 1.8 and 6, Fig. 13). These differences, although non negligible, are relatively small if we consider the great differences in the geomorphological settings of the two study areas and the hydrologic-hydraulic characteristics of the events that cause channel widening in northern Apennines and in the Stolla. Focusing the analysis on these predictive variables and extending the dataset to include more study cases could represent a step toward non-site specific equations for channel widening.

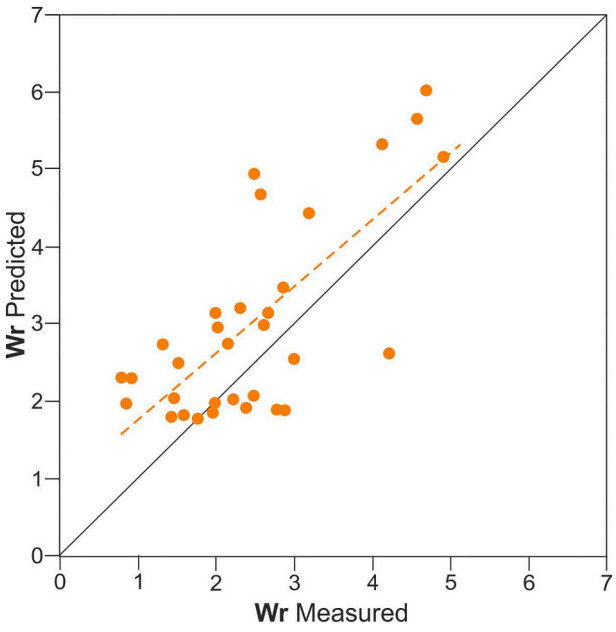

Fig. 13. Scatterplot of width ratios measured in this study (event I) and predicted using the equations proposed by Scorpio et al. (2018). Dashed line represents the regression line.

6. Conclusion

This study has analyzed the geomorphic effects in a mountain catchment caused by two storms characterized by different duration and rainfall intensities. During the infrequent, high-intensity (recurrence interval 200 years for rainfall duration of 1 h) event occurred in 2017, sediment supply originated from both fluvial processes (toe erosions and bed incision) as well as from several debris flows entering the channel. Landforms inducing sediment disconnection in respect to the main channel were represented by the hanging valleys and large debris cones at higher elevations and in the valley bottom, while talus slopes represented the main sediment supplies. During the - lower intensity (recurrence interval 4 years for rainfall duration of 1 h) - 2020 flood, sediment was transferred only along the main channel, as debris flows were not triggered on hillslopes. However, in both flood events, limited amounts of sediments were transferred to the catchment outlet, most probably due to the very short duration of the 2017 flood and to the relatively low flood magnitude for the 2020 storm. In both cases, the limiting factor for bedload export was hydrograph-related, as sediment supply was largely available, either from lateral (in 2017) or in-channel (2020) sources.

This study showed the important role of the landforms distribution in a catchment on constraining sediment delivery to both, the main channel and the basin outlet. In other words, it has confirmed that structural connectivity mainly controls sediment transport efficiency from upstream to downstream during high-intensity rainfall events, whereas low intensity storm determine a lack of functional connectivity between potential, structurally-connected debris flow channels.

New insights in the understanding of channel widening during extreme events indicate that the typology of channel widening – through bank erosions or overbank deposition – may reflect different characteristics of the valley confinement, channel geometry and flow energy, in particular bank erosion processes occurred mainly in narrow, steep and more confined reaches affected by higher unit stream power, whereas reaches prone to widening through overbank deposition presented less confined valley configurations and relative wider channels before and after the flood. Finally, this study confirms the role of the unit stream power and of the valley confinement in driving the channel adjustments controlling during flood events.

Declaration of competing interest

The authors declare that they have no known competing financial interests or personal relationships that could have appeared to influence the work reported in this paper.

Acknowledgments

This research was funded by the “CoupEvent: Hillslope - Channel coupling during extreme events in South Tyrol” supported by the Autonomous Province of Bozen-Bolzano (Bandi per la mobilitá di ricercatrici e ricercatori 2019). The authors thank the Department of Innovation, Research and University of the Autonomous Province of Bozen/Bolzano for covering the Open Access publication costs. MC, SC, and LM were supported by the project DTA.AD003.474 “Cambiamento climatico: mitigazione del rischio per uno sviluppo sostenibile”, funded by the Italian National Research Council. The 2010 DTM is part of the LiDAR survey by the Ministry for Environment, Land and Sea Protection of Italy of the Dolomitic area declared a World Heritage Site by UNESCO. 2014 orthophotos were made available by the Department of Geographic Informatics and Statistics of the Autonomous Province of Bolzano-Bozen. The Civil Protection Agency of the same Province is warmly thanked for making available their post-event analysis and photos.

The 2017 orthophotos and DTM were acquired thanks to the project SEDIPLAN-r (funded by UE EFRE-FESR 2014-2020 program and granted to the Free University of Bolzano-Bozen). 2020 orthophotos and LiDAR survey were funded by the project CoupEvent.

Finally, the authors are grateful to the reviewers, whose comments significantly improved the paper.

Appendix A. Supplementary data

Supplementary data to this article can be found online at https://doi.org/10.1016/j.geomorph.2022.108173.

References

Amponsah, W., Marchi, L., Zoccatelli, D., Boni, G., Cavalli, M., Comiti, F., Crema, S., Lucia, A.L., Marra, F., Borga, M., 2016. Hydrometeorological characterisation of a flash flood associated to major geomorphic effects: assessment of peak discharge uncertainties and analysis of the runoff response. J. Hydrometeorol. 17, 3063–3077. https://doi.org/10.1175/JHM-D-16-0081.1.

Baartman, J.E.M., Nunes, J.P., Masselink, R., Darboux, F., Bielders, C., Degré, A., Cantreul, V., Cerdan, O., Grangeon, T., Fiener, P., Wilken, F., Schindewolf, M., Wainwright, J., 2020. What do models tell us about water and sediment connectivity? Geomorphology 367, 107300. https://doi.org/10.1016/j.geomorph.2020.107300.

Bagnold, R.A., 1966. An approach to the sediment transport problem from general physics. US Geological Survey Professional Paper 422.

Benda, L., Dunne, T., 1997. Stochastic forcing of sediment routing and storage in channel networks. Water Resour. Res. 33 (12), 2865–2880.

Beylich, A., Brardinoni, F., 2013. Sediment sources, source-to-sink fluxes and sedimentary budgets. Geomorphology 188, 1–2.

Bertoldi, W., Zanoni, L., Tubino, M., 2010. Assessment of morphological changes induced by flow and flood pulses in a gravel bed braided river: the Tagliamento River (Italy). Geomorphology 114, 348–360.

Bracken, L.J., Turnbull, L., Wainwright, J., Bogaart, P., 2015. Sediment connectivity: a framework for understanding sediment transfer at multiple scales. Earth Surf. Process. Landf. 40, 177–188.

Brasington, J., Rumsby, B.T., McVey, R.A., 2000. Monitoring and modelling morphological change in a braided gravel-bed river using high resolution GPS-based survey. Earth Surf. Process. Landf. 25 (9), 973–990.

Boehner, J., Koethe, R., Conrad, O., Gross, J., Ringeler, A., Selige, T., 2002. Soil regionalisation by means of terrain analysis and process parameterisation. In: Micheli, E., Nachtergaele, F., Montanarella, L. (Eds.), Soil Classification 2001, Research Report No. 7, EUR 20398 EN. European Soil Bureau, Luxembourg, pp. 213–222.

Borga, M., Boscolo, P., Zanon, F., Sangati, M., 2007. Hydrometeorological analysis of the 29 August 2003 flash flood in the eastern Italian Alps. J. Hydrometeorol. 8, 1049–1067. https://doi.org/10.1175/JHM593.1.

Borga, M., Vezzani, C., Fontana, G.D., 2005. Regional rainfall depthduration-frequency equations for an Alpine region. Nat. Hazards 36, 221–235.

Boudevillain, B., Delrieu, G., Galabertier, B., Bonnifait, L., Bouilloud, L., Kirstetter, P.E., Mosini, M.L., 2011. The Cévennes-Vivarais Mediterranean Hydrometeorological Observatory database. Water Resour. Res. 47 (7), W07701.

Bracken, L.J., Turnbull, L., Wainwright, J., Bogaart, P., 2015. Sediment connectivity: a framework for understanding sediment transfer at multiple scales. Earth Surf. Process. Landf. 40 (2), 177–188.

Bracken, L.J., Wainwright, J., Ali, G.A., Tetzlaff, D., Smith, M.W., Reaney, S.M., Roy, A. G., 2013. Concepts of hydrological connectivity: research approaches, pathways and future agendas. Earth Sci. Rev. 119, 17–34. https://doi.org/10.1016/j.earscirev.2013.02.001.

Brardinoni, F., Mao, L., Recking, A., Rickenman, D., Turowski, J.M., 2015. Morphodynamics of steep montain channels. Earth Surf. Process. Landf. 40 (11), 1560–1562.

Brenna, A., Surian, N., Ghinassi, M., Marchi, L., 2020. Sediment–water flows in mountain streams: recognition and classification based on field evidence. Geomorphology 371, 107413.

Brenning, A., 2008. Statistical geocomputing combining R and SAGA: the example of landslide susceptibility analysis with generalized additive models. In: Hamburger Beiträge zur Physischen Geographie und Landschaftsökologie, 19, p. 410.

Brunsden, D., Thornes, J.B., 1979. Landscape sensitivity and change. Trans. Inst. Br. Geogr. 4, 463–484.

Bull, W.B., 1968. Alluvial fans. J. Geol. 16, 101–106.

Cavalli, M., Tarolli, P., Marchi, L., Dalla Fontana, G., 2008. The effectiveness of airborne LiDAR data in the recognition of channel-bed morphology. Catena 73 (3), 249–260. https://doi.org/10.1016/j.catena.2007.11.001.

Cavalli, M., Trevisani, S., Comiti, F., Marchi, L., 2013. Geomorphometric assessment of spatial sediment connectivity in small alpine catchments. Geomorphology 188, 31–41. https://doi.org/10.1016/j.geomorph.2012.05.007.

Cavalli, M., Goldin, B., Comiti, F., Brardinoni, F., Marchi, L., 2017. Assessment of erosion and deposition in steep mountain basins by differencing sequential digital terrain models. Geomorphology 291, 4–16.

Cavalli, M., Vericat, D., Pereira, P., 2019. Mapping water and sediment connectivity. Sci. Total Environ. 673, 763–767. https://doi.org/10.1016/j.scitotenv.2019.04.071.

Church, M., Jakob, M., 2020. What is a debris flood? Water Resour. Res. 56, e2020WR027144 https://doi.org/10.1029/2020WR027144.

Cislaghi, A., Bischetti, G.B., 2019. Source areas, connectivity, and delivery rate of sediments in mountainous-forested hillslopes: a probabilistic approach. Geomorphology 652, 1168–1186.

Comiti, F., Mao, L., 2012. Recent advances in the dynamics of steep channels. In: Church, M., Biron, P.M., Roy, A.G. (Eds.), Gravel-bed Rivers. https://doi.org/10.1002/9781119952497.ch26.

Cossart, É., Fressard, M., 2017. Assessment of structural sediment connectivity within catchments: insights from graph theory. Earth Surf. Dyn. 5, 253–268. https://doi.org/10.5194/esurf-5-253-2017.

Cossart, É., Viel, V., Lissak, C., Reulier, R., Fressard, M., Delahaye, D., 2018. How might sediment connectivity change in space and time? Land Degrad. Dev. 29, 2595–2613. https://doi.org/10.1002/ldr.3022.

Crema, S., Cavalli, M., 2018. SedInConnect: a stand-alone, free and open source tool for the assessment of sediment connectivity. Comput. Geosci. 111, 39–45. https://doi.org/10.1016/j.cageo.2017.10.009.

Cucchiaro, S., Cavalli, M., Vericat, D., Crema, S., Llena, M., Beinat, A., Marchi, L., Cazorzi, F., 2019. Geomorphic effectiveness of check dams in a debris-flow catchment using multi-temporal topographic surveys. Catena 174, 73–83. https://doi.org/10.1016/j.catena.2018.11.004.

Destro, E., Marra, F., Nikolopoulos, E.I., Zoccatelli, D., Creutin, J.D., Borga, M., 2017. Spatial estimation of debris flows–triggering rainfall and its dependence on rainfall return period. Geomorphology 278, 269–279. https://doi.org/10.1016/j.geomorph.2016.11.019.

De Walque, B., Degré, A., Maugnard, A., Bielders, C.L., 2017. Artificial surfaces characteristics and sediment connectivity explain muddy flood hazard in Wallonia. Catena 158, 89–101. https://doi.org/10.1016/j.catena.2017.06.016.

Eagle, L.J.B., Carrivick, J.L., Milner, A., Brown, L., Klaar, M., 2021. Repeated high flows drive morphological change in rivers in recently deglaciated catchments. Earth Surf. Process. Landforms. 46, 1294–1310.

Ferencevic, M.V., Ashmore, P., 2012. Creating and evaluating digital elevation modelbased stream-power map as a stream assessment tool. River Res. Appl. 28, 1394–1416.

Fryirs, K., 2013. (Dis)Connectivity in catchment sediment cascades: a fresh look at the sediment delivery problem. Earth Surf. Process. Landf. 38, 30–46.

Fryirs, K., 2017. River sensitivity: a lost foundation concept on fluvial geomorphology. Earth Surf. Process. Landf. 42, 55–70.

Fryirs, K.A., Brierley, G.J., Preston, N.J., Kasai, M., 2007. Buffers, barriers and blankets: the (dis)connectivity of catchment-scale sediment cascades. Catena 70 (1), 49–67.

Fryirs, K., Lisenby, P., Croke, J., 2015. Morphological resilience to catastrophic flooding: the case of Lockyer Creek, SE Queensland, Australia. Geomorphology 241, 55–71.

Gregoretti, C., Degetto, M., Bernard, M., Crucil, G., Pimazzoni, A., De Vido, G., Berti, M., Simoni, A., Lanzoni, S., 2016. Runoff of small rocky headwater catchments: Field observations and hydrological modeling. Water ResourRes. 52, 8138–8158. https://doi.org/10.1002/2016WR018675.

Grove, J.R., Croke, J., Thompson, C., 2013. Quantifying different riverbank erosion processes during 852 an extreme flood event. Earth Surf. Process. Landf. 38, 1393–1406.

Harvey, A.M., 2001. Coupling between hillslopes and channels in upland fluvial systems: implications for landscape sensitivity illustrated from the Howgill Fells, Northwest England. Catena 42, 225–250.

Hauer, C., Habersack, H., 2009. Morphodynamics of a 1000-year flood in the Kamp River, Austria, and impacts on floodplain morphology. Earth Surf. Process. Landf. 34, 654–682. https://doi.org/10.1002/esp.1763.

Heritage, G.L., Large, A.R.G., Moon, B.P., Jewitt, G., 2004. Channel hydraulics and geomorphic effects of an extreme flood event on the Sabie River, South Africa. Catena 58, 151–181.

Hooke, J.M., 2015. Variations in flood magnitude–effect relations and the implications for flood risk assessment and river management. Geomorphology 251, 91–107.

Jakob, M., 2005. A size classification for debris flows. Eng. Geol. 79, 151–161. https://doi.org/10.1016/j.enggeo.2005.01.006.

Jenkinson, A.F., 1955. The frequency distribution of the annual maximum (or minimum) values of meteorological elements. Quart. J. R. Meteor. Soc. 81, 158–171. https://doi.org/10.1002/qj.49708134804.

Knighton, A.D., 1999. Downstream variation in stream power. Geomorphology 29 (3–4), 293–306.

Krapesch, G., Hauer, C., Habersack, H., 2011. Scale orientated analysis of river width changes due to extreme flood hazard. Nat. Hazards Earth Syst. Sci. 11, 2137–2147.

Lane, S.N., Westaway, R.M., Hicks, D.M., 2003. Estimation of erosion and deposition volumes in a large, gravel-bed, braided river using synoptic remote sensing. Earth Surf. Process. Landf. 28, 249–271. https://doi.org/10.1002/esp.483.

Lallias-Tacon, S., Liébault, F., Piégay, H., 2014. Step by step error assessment in braided river sediment budget using airborne LiDAR data. Geomorphology 214, 307–323. https://doi.org/10.1016/j.geomorph.2014.02.014.

Leopold, L.B., Marchand, M.O., 1968. On the quantitative inventory of the riverscape. Water Resour. Res. 4, 709–717.

Lenzi, M.A., 2001. Step-pool evolution in the Rio Cordon, northeastern Italy. Earth SurfProcesses Landforms 26, 991–1008.

Lenzi, M.A., Mao, L., Comiti, F., 2004. Magnitude-frequency analysis of bed load data in an Alpine boulder bed stream. Water Resour. Res. 40, W07201. https://doi.org/10.1029/2003WR002961.

Liébault, F., Gomez, B., Page, M., Marden, M., Peacock, D., Richard, D., Trotter, C.M., 2005. Land-use change, sediment production and channel response in upland regions. River Res. Appl. 21, 1–18.

Llasat, M.C., Llasat-Botija, M., Prat, M.A., Porcu, F., Price, C., Mugnai, A., Lagouvardos, K., Kotroni, V., Katsanos, D., Michaelides, S., Yair, Y., Savvidou, K., Nicolaides, K., 2010. High-impact floods and flash floods in Mediterranean countries: the FLASH preliminary database. Adv. Geosci. 23, 47–55.

Llena, M., Vericat, D., Cavalli, M., Crema, S., Smith, M.W., 2019. The effects of land use and topographic changes on sediment connectivity in mountain catchments. Sci. Total Environ. 660, 899–912. https://doi.org/10.1016/j.scitotenv.2018.12.479.

Lucía, A., Comiti, F., Borga, M., Cavalli, M., Marchi, L., 2015. Dynamics of large wood during a flash flood in two mountain catchments. Nat. Hazards Earth Syst. Sci. 15, 1741–1755. https://doi.org/10.5194/nhess-15-1741-2015.

Lucía, A., Schwientek, M., Eberle, J., Zarfl, C., 2018. Planform changes and large wood dynamics in two torrents during a severe flash flood in Braunsbach, Germany 2016. Sci. Total Environ. 640–641, 315–326. https://doi.org/10.1016/j.scitotenv.2018.05.186.

Magilligan, F.J., 1992. Thresholds and the spatial variability of flood power during extreme floods. Geomorphology 5, 373–390.

Marchi, L., Dalla Fontana, G., Cavalli, M., Tagliavini, F., 2008. Rocky headwaters in the Dolomites, Italy: field observations and topographic analysis. Arct. Antarct. Alp. Res. 40 (4), 685–694.

Marra, F., Nikolopoulos, E.I., Creutin, J.D., Borga, M., 2014. Radar rainfall estimation for the identification of debris-flow occurrence thresholds. J. Hydrol. 519, 1607–1619. https://doi.org/10.1016/j.jhydrol.2014.09.039.

Marra, F., Morin, E., 2015. Use of radar QPE for the derivation of intensity–duration–frequency curves in a range of climatic regimes. J. Hydrol. 531, 427–440. https://doi.org/10.1016/j.jhydrol.2015.08.064.

Martens, B., Cabus, P., De Jongh, I., Verhoest, N.E.C, 2013. Merging weather radar observations with ground-based measurements of rainfall using an adaptive multiquadric surface fitting algorithm. J. Hydrol. 500, 84–96.

Messenzehl, K., Hoffmann, T., Dikau, R., 2014. Sediment connectivity in the high-alpine valley of Val Müschauns, Swiss National Park - linking geomorphic field mapping with geomorphometric modelling. Geomorphology 221, 215–229.

Minute, F., Comiti, F., Cavalli, M., 2019. Assessing geomorphic changes induced by a debris-flow: a case study in the Dolomites. Rend. Online Soc. Geol. It. 48, 23–28. https://doi.org/10.3301/ROL.2019.33.

Montgomery, D.R., Buffington, J.M., 1997. Channel-reach morphology in mountain drainage basins. Geol. Soc. Am. Bull. 109, 596–611.

Moore, R.J., 2007. The PDM rainfall-runoff model. Hydrol. Earth Syst. Sci. 11 (1), 483–499. https://doi.org/10.5194/hess-11-483-2007.

Morche, D., Schmidt, K.-H., Heckmann, T., Haas, F., 2006. Hydrology and geomorphic effects of a high-magnitude flood in an Alpine river. Geogr. Ann. 89 A (1), 5–19.

Nardi, L., Rinaldi, M., 2015. Spatio-temporal patterns of channel changes in response to a major flood event: the case of the Magra River (central-Northern Italy). Earth Surf. Process. Landf. 40, 326–339.

Otto, J.C., Schrott, L., Jaboyedoff, M., Dikau, R., 2009. Quantifying sediment storage in a high alpine valley (Turtmanntal, Switzerland). Earth Surf. Process. Landf. 34, 1726–1742.

Pellarin, T., Delrieu, G., Saulnier, G.M., 2002. Hydrologic visibility of weather radar systems operating in mountainous regions: case study for the Ardèche catchment (France). J. Hydrometeorol. 3, 539–555.

Pellegrini, G., Martini, L., Cavalli, M., Rainato, R., Cazorzi, A., Picco, L., 2021. The morphological response of the Tegnas alpine catchment (Northeast Italy) to a large Infrequent Disturbance. Sci. Total Environ. 145209 https://doi.org/10.1016/j.scitotenv.2021.145209.

Phillips, J.D., 2009. Changes, perturbations, and responses in geomorphic systems. Prog. Phys. Geogr. 33, 17–30.

Piégay, H., Chabot, A., Le Lay, Y.F., 2020. Some comments about resilience: from cyclicity to trajectory, a shift in living and nonliving system theory. Geomorphology 367, 106527. https://doi.org/10.1016/j.geomorph.2018.09.018.

Rainato, R., Picco, L., Cavalli, M., Mao, L., Neverman, A.J., Tarolli, P., 2018. Coupling climate conditions, sediment sources and sediment transport in an Alpine Basin. Land Degrad. Dev. 29, 1154–1166. https://doi.org/10.1002/ldr.2813.

R Development Core Team, 2020. A Language and Environment for Statistical Computing. R Foundation for Statistical Computing. https://www.R-project.org.

Rainato, R., Martini, L., Pellegrini, G., Picco, L., 2021. Hydrological, geomorphic and sedimentological responses of an alpine basin to a severe weather event (Vaia storm). Catena 207, 105600. https://doi.org/10.1016/j.catena.2021.105600.

Reid, S.M., Lane, S.N., Montgomery, D.R., Brookes, C., J., 2007. Does hydrological connectivity improve modelling of coarse sediment delivery in upland environments? Geomorphology 90 (3–4), 263–282. https://doi.org/10.1016/j.geomorph.2006.10.023.

Rickenmann, D., Koschni, A., 2010. Sediment loads due to fluvial transport and debris flows during the 2005 flood events in Switzerland. Hydrol. Process. 24 (993–1007), 2010. https://doi.org/10.1002/hyp.7536.

Reinfelds, I., Cohen, T., Batten, P., Brierley, G., 2004. Assessment of Downstream Trends in Channel Gradient, Total and Specific Stream Power: A GIS Approach. Geomorphology 60 (3–4), 403–416.

Rickenmann, D., Badoux, A., Hunzinger, L., 2016. Significance of sediment transport processes during piedmont floods: the 2005 flood events in Switzerland. Earth Surf. Proc. Landf. 230 (224–230), 2016. https://doi.org/10.1002/esp.3835.

Rinaldi, M., Surian, N., Comiti, F., Bussettini, M., 2013. A method for the assessment and analysis of the hydromorphological condition of italian streams: the Morphological Quality Index (MQI). Geomorphology 180–181, 96–108.

Rinaldi, M., Gurnell, A.M., Belletti, B., Berga Cano, M.I., Bizzi, S., Bussettini, M., Gonzalez del Tanago, M., Grabowski, R., Habersack, R., Klösch, M., Mosselman, E., Toro Velasco, M., Vezza, P., Magdaleno Mas, F., 2015. Final report on methods, models, tools to assess the hydromorphology of rivers. In: Deliverable 6.2, Part 1, of REFORM (REstoring rivers FOR effective catchment Management), a Collaborative Project (Large-scale Integrating Project) Funded by the European Commission Within the 7th Framework Programme under Grant Agreement282656.

Rinaldi, M., Amponsah, W., Benvenuti, M., Borga, M., Comiti, F., Lucìa, A., Marchi, L., Nardi, L., Righini, M., Surian, N., 2016. An integrated approach for investigating geomorphic response to extreme events: methodological framework and application to the October 2011 flood in the Magra River catchmentItaly. Earth Surf. Process. Landf. 41, 835–846. https://doi.org/10.1002/esp.3902.

Righini, M., Surian, N., Wohl, E., Marchi, L., Comiti, F., Amponsah, W., Borga, M., 2017. Geomorphic response to an extreme flood in two Mediterranean rivers (northeastern Sardinia, Italy): analysis of controlling factors. Geomorphology 290, 184–199.

Roux, C., Alber, A., Bertrand, M., Vaudor, L., Piégay, H., 2015. "FluvialCorridor": a new ArcGIs toolbox package for multiscale riverscape exploration. Geomorphology 242, 29–37.

Ruiz-Villanueva, V., Badoux, A., Rickenmann, D., Böckli, M., Schläfli, S., Steeb, N., Stoffel, M., Rickli, C., 2018. Impacts of a large flood along a mountain river basin: the importance of channel widening and estimating the large wood budget in the upper Emme River (Switzerland). Earth Surf. Dyn. 6, 1115–1137. https://doi.org/10.5194/esurf-6-1115-2018.

Schumm, S.A., 1991. To Interpret the Earth: Ten Ways to Be Wrong. Cambridge University Press, Cambridge.

Santangelo, N., Daunis-i-Estadella, J., Di Crescenzo, G., Di Donato, V., Faillace, P., Martin-Fernandez, J.A., Romano, P., Santo, A., Scorpio, V., 2012. Topographic predictors of susceptibility to alluvial fan flooding, Southern Apennines. Earth Surf. Proc. Landf. 37, 803–817. https://doi.org/10.1002/esp.3197.

Santo, A., Santangelo, N., Di Crescenzo, G., Scorpio, V., De Falco, M., Chirico, G.B., 2015. Flash flood occurrence and magnitude assessment in an alluvial fan context: the October 2011 event in the Southern Apennines. Nat. Hazard. 78, 417–442. https://doi.org/10.1007/s11069-015-1728-4.

Stoffel, M., Wyżga, B., Marston, R.A., 2016. Floods in mountain environments: a synthesis. Geomorphology 272, 1–9.

Surian, N., Righini, M., Lucía, A., Nardi, L., Amponsah, W., Benvenuti, M., Borga, M., Cavalli, M., Comiti, F., Marchi, L., Rinaldi, M., Viero, A., 2016. Channel response to extreme floods: insights on controlling factors from six mountain rivers in northern Apennines, Italy. Geomorphol. Floods Mt. Environ. 272, 78–91. https://doi.org/10.1016/j.geomorph.2016.02.002.

Schaffrath, K.R., Belmont, P., Wheaton, J.M., 2015. Landscape-scale geomorphic change detection: quantifying spatially variable uncertainty and circumventing legacy data issues. Geomorphology 250, 334–348. https://doi.org/10.1016/j.geomorph.2015.09.020.

Schopper, N., Mergili, M., Frigerio, S., Cavalli, M., Poeppl, R., 2019. Analysis of lateral sediment connectivity and its connection to debris flow intensity patterns at different return periods in the Fella River system in northeastern Italy. Sci. Total Environ. 658, 1586–1600.

Schuerch, P., Densmore, A.L., McArdell, B.W., Molnar, P., 2006. The influence of landsliding on sediment supply and channel change in a steep mountain catchment. Geomorphology 78, 222–235.

Schmidt, K.H., Morche, D., 2006. Sediment output and effective discharge in two small high mountain catchments in the Bavarian Alps, Germany. Geomorphology 80, 131–145.

Scorpio, V., Crema, S., Marra, F., Righini, M., Ciccarese, G., Borga, M., Cavalli, M., Corsini, A., Marchi, L., Surian, N., Comiti, F., 2018. Basin-scale analysis of the geomorphic effectiveness of flash floods: a study in the northern Apennines (Italy). Sci. Total Environ. 640–641, 337–351. https://doi.org/10.1016/j.scitotenv.2018.05.252.

Scorpio, V., Piégay, H., 2021. Is afforestation a driver of change in italian rivers within the Anthropocene Era? Catena 198, 105031. https://doi.org/10.1016/j.catena.2020.105031.

Scorpio, V., Santangelo, N., Santo, A., 2016. Multiscale map analysis in alluvial fan flood-prone areas. Journal of Maps 12 (2), 382–393. https://doi.org/10.1080/17445647.2015.1027155.

Shmilovitz, Y., Morin, E., Rinat, Y., Haviv, I., Carmi, G., Mushkin, A., Enzel, Y., 2020. Linking frequency of rainstorms, runoff generation and sediment transport across hyperarid talus-pediment slopes. Earth Surf. Process. Landf. 49 (7), 1644–1659.

Steger, S., Brenning, A., Bell, R., 2016. Exploring discrepancies between quantitative validation results and the geomorphic plausibility of statistical landslide susceptibility maps. Geomorphology 262, 8–23.

Steger, S., Mair, V., Kofler, C., Pittore, M., Schneiderbauer, S., Zebisch, M., 2021. A statistical exploratory analysis of inventoried slide-type movements for south Tyrol (Italy). In: Guzzetti, F., Mihalić Arbanas, S., Reichenbach, P., Sassa, K., Bobrowsky, P.T., Takara, K. (Eds.), Understanding and Reducing Landslide Disaster Risk. WLF 2020. ICL Contribution to Landslide Disaster Risk Reduction. Springer, Cham.

Stockner, K., 2019. Gemeinde Prags - Landschaftsplan; Comune di Braies - Piano paesaggistico. Retrieved 08/11/19. http://gis2.provinz.bz.it/mapAccel/docs/Landbrowser_docs/ErlauterndeBerichte_DE/69_erb.pdf.

Surian, N., Mao, L., Giacomin, M., Ziliani, L., 2009. Morphological effects of different channel-forming discharges in a gravel-bed river. Earth Surf. Process. Landforms 34, 1093–1107. https://doi.org/10.1002/esp.1798.

Tarolli, P., Borga, M., Morin, E., Delrieu, G., 2012. Analysis of flash flood regimes in the north-western and South-Eastern Mediterranean regions. Nat. Hazards Earth Syst. Sci. 12, 1255–1265.

Thompson, C., Croke, J., 2013. Geomorphic effects, flood power, and channel competence of a catastrophic flood in confined and unconfined reaches of the upper Lockyer valley, Southeast Queensland, Australia. Geomorphology 197, 156–169.

Thompson, C., Fryirs, K., Croke, J., 2016. The disconnected sediment conveyor belt: patterns of longitudinal and lateral erosion and deposition during a catastrophic flood in the Lockyer Valley, southeast Queensland. Australia. River Research and Applications. https://doi.org/10.1002/rra.2897.

Tiranti, D., Cavalli, M., Crema, S., Zerbato, M., Graziadei, M., Barbero, S., Cremonini, R., Silvestro, C., Bodrato, G., Tresso, F., 2016. Semi-quantitative method for the assessment of debris supply from slopes to river in ungauged catchments. Sci. Total Environ. 554–555, 337–348. https://doi.org/10.1016/j.scitotenv.2016.02.150.

Toone, J., Rice, S.P., Piégay, H., 2012. Spatial discontinuity and temporal evolution of channel morphology along a mixed bedrock-alluvial river, upper Drôme River, Southeast France: contingent responses to external and internal controls. Geomorphology. https://doi.org/10.1016/j.geomorph.2012.05.033.

Turowski, J.M., Yager, E.M., Badoux, A., Rickenmann, D., Molnar, P., 2009. The impact of exceptional events on erosion, bedload transport and channel stability in a step-pool channel. Earth Surf. Process. Landf. 34, 1661–1673.

Vericat, D., Wheaton, J.M., Brasington, J., 2017. Revisiting the morphological approach: opportunities and challenges with repeat high-resolution topography. In: Tsutsumi, D., Laronne, J.B. (Eds.), Gravel-bed Rivers Processes and Disasters. John Wiley and Sons, Chichester, pp. 121–158.

Villarini, G., Mandapaka, P.V., Krajewski, W.F., Moore, R.J., 2008. Rainfall and sampling uncertainties: a rain gaugeperspective. J. Geophys. Res. 113, D11102. https://doi.org/10.1029/2007JD009214.

Walling, D.E., 1983. The sediment delivery problem. J. Hydrol. 65 (1–3), 209–237.

Wainwright, J., Turnbull, L., Ibrahim, T.G., Lexartza-Artza, I., Thornton, S.F., Brazier, R., 2011. Linking environmental régimes, space and time: interpretations of structural and functional connectivity. Geomorphology 126 (3–4), 387–404. https://doi.org/10.1016/j.geomorph.2010.07.027.

Wheaton, J.M., Brasington, J., Darby, S.E., Sear, D.A., 2010. Accounting for uncertainty in DEMs from repeat topographic surveys: improved sediment budgets. Earth Surf. Process. Landf. 35, 136–156. https://doi.org/10.1002/esp.1886.

Wohl, E., Brierley, G., Cadol, D., Coulthard, T.J., Covino, T., Fryirs, K.A., Grant, G., Hilton, R.G., Lane, S.N., Magilligan, F.J., Meitzen, K.M., Passalacqua, P., Poeppl, R. E., Rathburn, S.L., Sklar, L.S., 2019. Connectivity as an emergent property of geomorphic systems. Earth Surf. Process. Landf. 44, 4–26.